Journal Pre-proofs

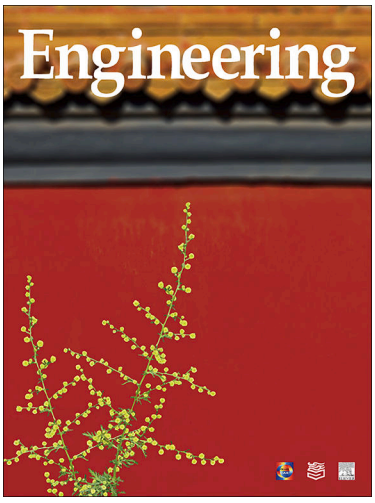

Article

Superiority of Secondary Bypass Air in an Integrated Thermal Management System: A Multi-Level Simulation Study

Jie Wen, Mengchen Li, Guoqiang Xu, Bensi Dong, Zhiwei Liu, Lei Chen, Laihe Zhuang

PII: S2095-8099(26)00185-2
DOI: https://doi.org/10.1016/j.eng.2026.03.017
Reference: ENG 2311

To appear in: *Engineering*

Received Date: 28 May 2025
Revised Date: 4 March 2026
Accepted Date: 26 March 2026

Please cite this article as: J. Wen, M. Li, G. Xu, B. Dong, Z. Liu, L. Chen, L. Zhuang, Superiority of Secondary Bypass Air in an Integrated Thermal Management System: A Multi-Level Simulation Study, *Engineering* (2026), doi: https://doi.org/10.1016/j.eng.2026.03.017

Research
Journal Pre-proofs
Green Aviation Propulsion—Article

Superiority of Secondary Bypass Air in an Integrated Thermal Management System: A Multi-Level Simulation Study

Jie Wen[a,b,e], Mengchen Li[a,b,e], Guoqiang Xu[a,b,e], Bensi Dong[c,e], Zhiwei Liu[b], Lei Chen[d], Laihe Zhuang[a,b,e,*]
[a] *Research Institute of Aero-engine, Beihang University, Beijing 100191, China*
[b] *International Innovation Institute, Beihang University, Hangzhou 310023, China*
[c] *School of Energy and Power Engineering, Beihang University, Beijing 100191, China*
[d] *AECC Sichuan Gas Turbine Establishment, Chengdu 610500, China*
[e] *Frontiers Science Center for Super-cycle Aeroengine's Aerothermodynamics, Beihang University, Beijing 100191, China*
* Corresponding author. Email: zhuanglaihe@buaa.edu.cn

A novel simulating model is developed by integrating the VCE and FTMS system
The superiority of multi heat sink is quantitative revealed within typical missions
The allocation strategies of different heat-exchange area are discussed

ABSTRACT

With the advancement of next-generation fighter aircraft, the escalating cooling demands of thermal management in aircraft and their engines are approaching the thresholds of conventional heat sinks, including ram air and fuel. A variable cycle engine (VCE), characterized by its third-stream design, facilitates potential multi-heat sink coordination within the fuel thermal management system (FTMS). Despite the use of decoupled VCE and FTMS modeling in previous research, the heat sink potential of internal secondary bypass air remains largely unexplored and unquantified, with its feedback effects on VCE energy efficiency also lacking rigorous investigation. Driven by the background, this study proposes a novel coupling of VCE and FTMS design. By leveraging multidisciplinary simulations, we provide the first quantitative analysis of the heat sink efficacy of secondary bypass air across representative flight missions and elucidate its synergistic mechanism with fuel. Investigations reveal that compared with ram air, secondary bypass air markedly reduces the thermal accumulation by 36.57%–74.06%. This improved thermal performance is accompanied by a 2.17%–4.10% decrease in the hot-return fuel flow. Intriguingly, the induced specific fuel consumption penalty throughout various typical flight missions consistently remains below 0.8%, thereby demonstrating the economic efficiency and sustainable benefits of employing secondary bypass air for thermal management. Furthermore, this study presents the first optimization strategy for allocating heat transfer areas. Specifically, an area ratio of 0.6 between the ram air and secondary bypass air significantly lowers the system hot-return fuel temperature by 2.68%. This work validates quantitative evidence for secondary bypass air–FTMS coupling and establishes a foundation for system-level thermal management schemes in advanced fighter aircraft and engine designs.
Keywords: Fuel thermal management system, Variable cycle engine, Secondary bypass air, Coupling mechanism, Multi-level analysis

1 Introduction

In recent years, the development of effective fuel thermal management systems (FTMS) has emerged as a critical challenge for advanced aeroengines. The rising thermal loads from aircraft systems, such as environmental control and engine lubrication, necessitate enhanced cooling performance of the fuel [1–3]. Concurrently, the improved fuel efficiency of advanced aeroengines markedly diminishes the heat-dissipating capacity of the combustion process [4,5]. Consequently, FTMS-related thermal management challenges are becoming increasingly severe and are now critical research priorities in aeroengine design.

An FTMS is a universal system for addressing thermal loads in aeroengines and primarily comprises essential components such as pipelines, fuel pumps, heat exchangers, and control valves [6]. The waste heat absorbed by the FTMS can be dissipated via three primary pathways: burning in the combustion chamber, transferring heat to the auxiliary heat sinks, and returning to the aircraft fuel tank. In the first pathway, the coking temperature of the fuel limits its cooling capability. Therefore, several studies have focused on defining the maximum permissible temperature for various fuel types. Tao et al. [7] investigated the coking characteristics of RP-3 aviation kerosene and revealed that fuel coking occurred on the surfaces of microfine circular metal tubes at 423.15 K. The United Technologies Research Center [8,9] exploited the endothermic potential of JP-7 and JP-8 + 100 to improve the heat sink performance of the fuel by increasing its coking temperature. As the thermal loads in advanced aircraft engines increase, the intrinsic cooling capacity of the fuel becomes insufficient, making the deployment of supplementary heat sinks imperative for dissipating excessive thermal loads [10]. In the second pathway, ram air was once widely employed as an auxiliary heat sink. However, its utilization incurs notable drawbacks, including increased specific fuel consumption, thrust loss, and reduced stealth capability [11]. These disadvantages ultimately restrict its application in advanced aircraft and engine systems [12].

When the two approaches mentioned above (fuel cooling and ram air systems) are inadequate to meet the cooling demands, a third strategy is adopted: recirculation of the heated fuel back to the aircraft's fuel tanks [13,14]. While it seems ostensibly effective, it inevitably compromises the fuel-cooling capacity across the entire flight mission, as heat is merely transferred to the fuel tank without being dissipated to the environment. To address these inherent challenges, substantial advancements have been made in the design of thermal management architectures to seek more effective methods of dissipating excess heat. Shi et al. [15] proposed an intelligent method based on a backtracking algorithm to enable automated generation and exploration of an architectural space. This method allows the systematic generation of a range of thermal management system architectures, thereby providing an efficient pathway for optimizing the design of complex thermal management systems.

Sigthorsson et al. [16,17] developed an innovative dual-tank topology that demonstrated a 35% enhancement in thermal endu tank framework incorporating hot and cold reuse tanks. Building on these architectures, researchers [20–24] further formulated adaptive control strategies. These strategies dynamically reconfigure the FTMS flow path topology according to the real-time flight conditions, thereby enabling the selection of an optimal FTMS architecture specifically tailored to the distinct heat dissipation requirements and capabilities of various flight missions. In addition, intelligent control algorithms have been extended to energy management systems across full mission profiles, effectively improving the aircraft's energy utilization efficiency [25]. Progress in optimization algorithms has also enabled Yang et al. [26] to propose a dynamic control strategy. Through optimized flow path management, this strategy demonstrated a 14.16% reduction in the system return fuel temperature.

Prior research has partially enhanced the heat-dissipation performance of FTMS. However, its intrinsic limitation lies in the persistent emphasis on maximizing the intrinsic heat absorption capacity of the fuel, which inherently restricts its capacity to transcend the theoretical thresholds of fuel-based heat dissipation. Increasing aeroengine thermal loads continuously overwhelm the cooling capacity of the fuel alone, thereby perpetuating the issue of insufficient FTMS cooling. Considering this, it is of paramount importance to pursue innovative strategies to address the thermal management challenges in FTMS through the incorporation of auxiliary heat sinks. For instance, Yu et al. [27] devised a vapor compression system that converted the lubricant's thermal load into the internal energy of R134a, thereby lessening the lubricant's cooling demand on the kerosene fuel. Similarly, Chen et al. [28] and Johnson et al. [29] independently explored the utilization of cryogenic working media such as supercritical nitrogen and ammonium carbamate as expendable heat sinks to mitigate insufficient fuel-cooling capacity. Despite their potential to improve the cooling efficacy, these methodologies invariably introduce inherent drawbacks, including increased system complexity, considerable flow resistance, and diminished system stability. Consequently, to avoid the aforementioned issue of additional flow resistance, an integrated structural design was developed, wherein the static vanes of the ducted fan were ingeniously employed for waste heat utilization [30].

Compared with ram air and cryogenic media, secondary bypass air stands out as an excellent heat sink, primarily due to its inherent advantage of providing extra cooling capacity without imposing a mass penalty. Additionally, the advantage of utilizing secondary bypass air is further underscored during the subsonic cruise, where its mass flow rate reaches its peak, coinciding with minimum fuel consumption [31]. This characteristic implies that the scenario of minimum fuel-cooling performance aligns precisely with the period during which the secondary bypass air exhibits its peak heat sink capability. Dooley et al. [32] emphasized the significant appeal of secondary bypass air for military aeroengines, attributing this to its inherent capacity for waste heat dissipation. In terms of quantitative assessment, Simmons [33] developed a simulation model of a third-stream variable cycle engine (VCE) and determined that the secondary bypass air possessed the capacity to absorb nearly one megawatt of thermal load. Nonetheless, their model omitted consideration of realistic heat transfer processes or fluid flow resistance limitations. Clark et al. [34] assessed the heat transfer efficiency to calculate the practical heat transfer capacity between secondary bypass air and thermal loads. However, the effect of flow resistance induced by the heat transfer process remained unanalyzed.

Accordingly, previous research has examined fuel and ram air as FTMS heat sinks and has also recognized secondary bypass air from VCE as a promising alternative [31,32]. However, these investigations were largely confined to thermodynamic availability analyses based on energy balance equations, thereby neglecting the performance impacts of actual heat transfer processes and flow resistance constraints on the integrated VCE–FTMS system [33]. Besides, the few analyses that accounted for heat transfer typically employed a constant heat transfer effectiveness [34], precluding the quantitative evaluation of the heat sink's potential under varying mission conditions. Therefore, this study pioneers an integrated multi-level analysis model that simultaneously considers both the VCE and FTMS. The purpose of this novel model is to analyze the fundamental mechanisms by which secondary bypass air influences the performance of the VCE and FTMS. First, based on an integrated aircraft engine simulation during a typical flight mission, a comparative analysis was conducted between a conventional thermal management scheme utilizing ram air as the heat sink and a novel approach employing secondary bypass air. Subsequently, different heat sink-based fuel thermal management strategies were comprehensively evaluated based on their holistic performance throughout the full flight envelope. This comparison encompassed heat-dissipation performance, heat sink efficiency, and overall performance implications. The primary aim was to identify the best-performing scheme under specific operational flight conditions. Ultimately, the design parameters for both the fuel–ram air and fuel–bypass air heat exchangers were selected as independent variables to evaluate the performances of both the VCE and FTMS under various design schemes.

2 Description of VCE and FTMS integrated architecture

2.1 Framework analysis

The integrated VCE and FTMS framework is depicted in Fig. 1.

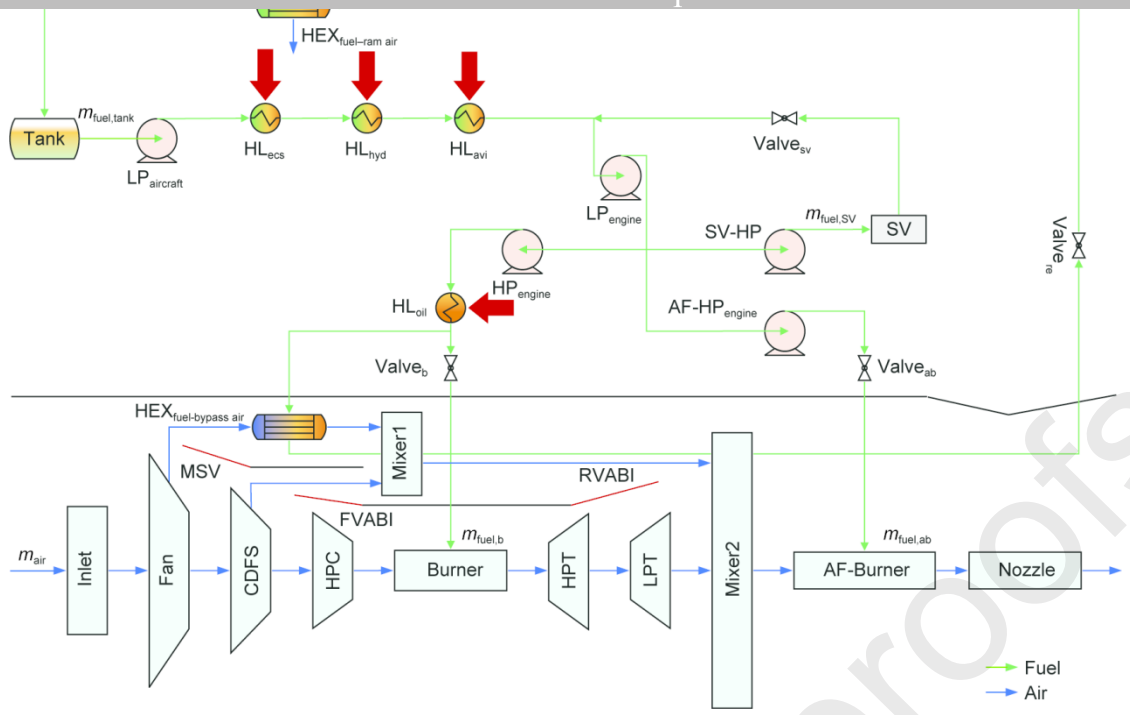

Fig. 1. Schematic of VCE and FTMS. The employed abbreviations are defined in the main text and the Nomenclature.

Compared with the original aeroengine, the modified design incorporates three adjustable valves, including the mode selection valve (MSV), front variable area bypass injector (FVABI), and rear variable area bypass injector (RVABI), which can affect the VCE working mode. The operational state of the MSV dictates whether the VCE operates in double- or single-bypass mode. The opening of the FVABI valve affects the distribution of air flowing into the core engine and secondary bypass. The working conditions of the RVABI also considerably modulate the flow velocity of the gas in front of the mixer. The secondary bypass air is employed as an additional heat sink in the fuel-bypass air heat exchanger ($HEX_{fuel–bypass\ air}$) for the FTMS. An FTMS is typically modeled as an energy system featuring a multiloop topological network. Once pressurized by a low-pressure fuel pump ($LP_{aircraft}$), the fuel successively absorbs thermal loads from the environmental control (HL_{ecs}), hydraulic (HL_{hyd}), and avionics (HL_{avi}) systems, and then flows into the engine. The flow is pressurized by a low-pressure fuel pump (LP_{engine}) and divided into three streams: One passes through a high-pressure fuel pump (HP_{engine}), absorbs thermal loads from the lubricating oil (HL_{oil}), and then flows into the burner; another is directed to the afterburner through the afterburner fuel pump ($AF\text{-}HP_{engine}$); and the final one is supplied to the servo actuation system through a servo high-pressure fuel pump (SV-HP). In the FTMS, fuel can be utilized through combustion, whereas excess fuel must be returned to the tank through a branch in front of the burner inlet. Along the fuel return path, the hot fuel is cooled by the fuel–bypass air or fuel–ram air heat exchangers.

2.2 Evaluation based on energy interaction analysis

The energy utilization in the integrated system is illustrated in Fig. 2. Based on the mass and energy interactions between the VCE and FTMS, three interfaces for thermodynamic parameter transmission are established.

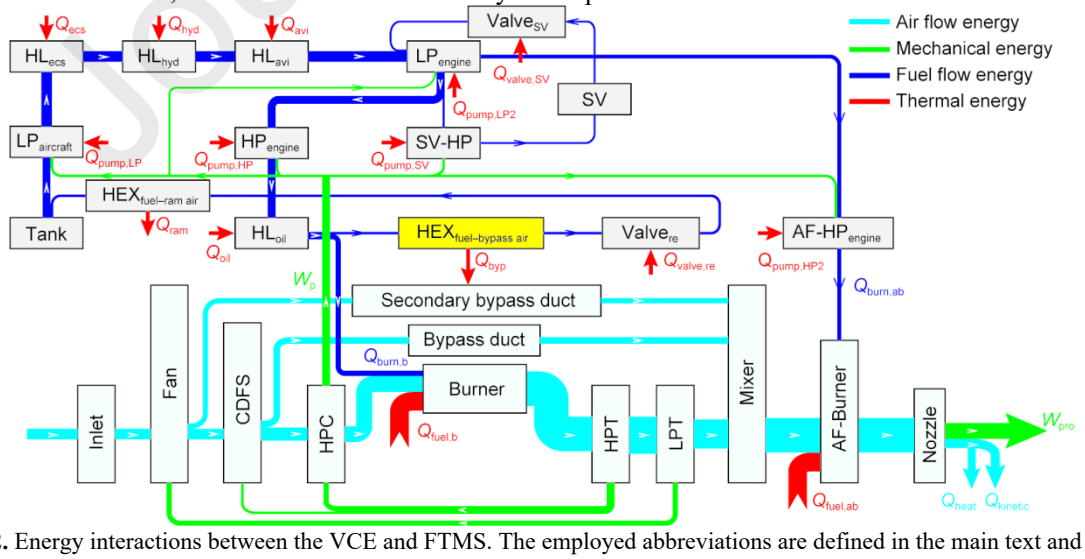

Fig. 2. Energy interactions between the VCE and FTMS. The employed abbreviations are defined in the main text and the Nomenclature.

(1) Mass flow from the FTMS to the VCE. The mass flow rate delivered from the FTMS to the VCE is directly regulated by t[Journal Pre-proofs]oint of thermal management, the mass flow rate of the fuel designated for combustion defines the baseline cooling capability in the absence of a hot-return fuel.

(2) Mechanical power transmission between the VCE and FTMS. In the VCE, the high-pressure turbine (HPT) converts the enthalpy of the combusted gas into mechanical energy. Most of the energy is used to drive the high-pressure compressor (HPC) and core-driven fan stage (CDFS), while a fraction is extracted as off-take power for accessories in the FTMS, including $LP_{aircraft}$, LP_{engine}, HP_{engine}, SV-HP, and $AF\text{-}HP_{engine}$. The pump speed depends on the VCE performance calculation model and can be correlated with the characteristic map of the pump to deduce its power and efficiency.

(3) Heat exchange between the VCE and FTMS. The secondary bypass air serves as the primary heat sink for the integrated system, which cools the hot-return fuel from the FTMS in the $HEX_{fuel–bypass\ air}$. The thermodynamic parameters of the fuel and bypass air at the inlet can be derived from the integrated VCE and FTMS performance simulation under given working conditions. Subsequently, using the heat exchanger performance model, one can precisely evaluate the flow and heat transfer characteristics of $HEX_{fuel–bypass\ air}$.

In the VCE, air enters the aeroengine through the inlet, and the input energy is the chemical energy of the fuel (Q_{fuel}) and heat load from the secondary bypass air (Q_{byp}) in the FTMS. Energy is converted into different forms, such as propelling power (W_{pro}) for engine flight, shaft power (W_p) transferred to the FTMS, exhaust gas heat loss (Q_{heat}), and kinetic energy loss ($Q_{kinetic}$). The energy conservation equation of the VCE can be defined as [35]

$$Q_{fuel,b} + Q_{fuel,ab} + Q_{byp} = W_{pro} + W_p + Q_{heat} + Q_{kinetic} \quad (1)$$

$$Q_{fuel} = \eta_b(m_{fuel,b} + m_{fuel,ab})\mathrm{LHV} \quad (2)$$

$$W_{pro} = FV_{aircraft} \quad (3)$$

$$Q_{kinetic} = \frac{1}{2}(m_{air} + m_{fuel,b} + m_{fuel,ab})(V_{out} - V_{aircraft})^2 \quad (4)$$

$$Q_{heat} = (m_{air} + m_{fuel,b} + m_{fuel,ab})(h_{out} - h_{in}) \quad (5)$$

where η_b is the combustion efficiency of the burner; LHV is the lower heating value of fuel; $m_{fuel,b}$, $m_{fuel,ab}$, and m_{air} are the fuel flow rate to the burner, the fuel flow rate to the afterburner, and the inlet air flow rate, respectively; F is the engine thrust; $V_{aircraft}$ and V_{out} are the velocities of the aircraft and exhaust gas, respectively; h_{in} and h_{out} are the specific enthalpies of inlet air and exhaust gas, respectively.

In aircraft engine performance analysis, the total thrust F and specific fuel consumption SFC are the most universal factors, whose definitions are as follows:

$$F = (m_{air} + m_{fuel,b} + m_{fuel,ab})V_{out} - m_{air}V_{aircraft} + (p_{out} - p_e)A_9 \quad (6)$$

$$\mathrm{SFC} = \frac{m_{fuel,b} + m_{fuel,ab}}{F} \quad (7)$$

where p_{out} is the nozzle outlet pressure; p_e is the environmental pressure; A_9 is the nozzle outlet area, respectively.

Within the FTMS, fuel is drawn from the tank and serves as a primary heat sink, absorbing heat loads from aircraft systems, including environmental control (Q_{ecs}), hydraulic (Q_{hyd}), and avionics (Q_{avi}) systems. Subsequently, the fuel undergoes further pressurization via low-pressure and high-pressure pumps in the engine, simultaneously cooling these pumps (Q_{pump}) and hot lubricating oil (Q_{oil}) and passing through the valves (Q_{valve}). The total heat load of these processes is denoted by Q_{load}.

$$Q_{load} = Q_{ecs} + Q_{hyd} + Q_{avi} + Q_{pump} + Q_{valve} + Q_{oil} \quad (8)$$

After absorbing the heat loads, the fuel is partly burned in the engine (Q_{burn}), and the remaining part returns to the tank. The accumulated heat (Q_{acc}) consists of two parts: The major portion is stored in the fuel tank via the hot-return fuel, and the remaining portion is absorbed by the components, including the pipes of the FTMS. To control the heat accumulation of return fuel, heat exchangers are installed in the return fuel loop, and heat can be transferred from the fuel to the secondary bypass air (Q_{byp}) or ram air (Q_{ram}). The energy conservation equations for the fuel are as follows:

$$Q_{load} = Q_{dis} + Q_{acc} \quad (9)$$

$$Q_{dis} = Q_{burn} + Q_{ram} + Q_{byp} \quad (10)$$

where Q_{dis} is the heat dissipation.

According to the energy conservation equation, it can be concluded that heat disposition can be achieved through ① burning, ② heat release into the heat sinks (e.g., bypass and ram air), and ③ heat storage in hot-return fuel and components.

Based on the normalization analysis, the dimensionless form of the governing equation can be obtained as

$$\frac{Q_{burn}}{Q_{load}} + \frac{Q_{ram}}{Q_{load}} + \frac{Q_{byp}}{Q_{load}} + \frac{Q_{acc}}{Q_{load}} = \xi_{burn} + \xi_{ram} + \xi_{byp} + \xi_{acc} = 1 \quad (11)$$

Here, ξ_{burn}, ξ_{ram}, ξ_{byp}, and ξ_{acc} represent the proportions of different heat disposition pathways, which are the criteria used to evaluate heat handling capability.

The FTMS should be designed to maximize ξ_{burn} by enhancing the utilization of combustion for heat dissipation. To achieve this goal, the fuel temperature should be elevated as close as possible to the coking threshold, yet remain below it. Consequently, the required heat accumulation within the system is alleviated with the help of auxiliary heat sinks, thereby reducing ξ_{acc}. The effectiveness of fuel cooling, defined by Eq. (12), quantifies the utilization of fuel as a heat sink and is

calculated as the heat dissipation through burning divided by the total heat absorption capacity of the fuel supplied to the FTM[redacted]al in addressing heat dissipation requirements throughout the flight mission.

$$R_{\mathrm{EFF}} = \frac{Q_{\mathrm{burn}}}{\max[Q_{\mathrm{in}}]} = \frac{c_p m_{\mathrm{fuel,b}}(T_{\mathrm{fuel,b}} - T_{\mathrm{fuel,in}})}{c_p m_{\mathrm{fuel,tank}}(T_{\mathrm{fuel,limit}} - T_{\mathrm{fuel,in}})} \quad (12)$$

$$R_{\mathrm{RES}} = \frac{E_{\mathrm{tank}}}{E_{\mathrm{tank,0}}} = \frac{c_p M_{\mathrm{tank}}(T_{\mathrm{fuel,limit}} - T_{\mathrm{fuel,tank}})}{c_p M_{\mathrm{tank,0}}(T_{\mathrm{fuel,limit}} - T_{\mathrm{fuel,tank,0}})} \quad (13)$$

where Q_{in} is the maximum heat absorption capacity of the fuel supplied to the FTMS; $m_{\mathrm{fuel,b}}$ and $m_{\mathrm{fuel,tank}}$ are the fuel flow rate for combustion and total fuel flow rate supplied to the FTMS, respectively; $T_{\mathrm{fuel,b}}$, $T_{\mathrm{fuel,in}}$, and $T_{\mathrm{fuel,limit}}$ are the fuel combustion temperature, fuel supply temperature, and maximum allowable fuel temperature, respectively; E_{tank} and $E_{\mathrm{tank,0}}$ are the maximum heat absorption capacities of the fuel stored in the tank at the current time and initial stage of the mission, respectively; M_{tank} and $M_{\mathrm{tank,0}}$ are the masses of fuel in the tank at the current time and initial stage, respectively; $T_{\mathrm{fuel,tank}}$ and $T_{\mathrm{fuel,tank,0}}$ are the temperature of the fuel in the tank at the current time and initial stage, respectively.

To summarize, the FTMS evaluation indices are presented in Table 1. The influence of the FTMS on the overall VCE performance is assessed using total thrust and specific fuel consumption. The cooling performance of FTMS is analyzed from different perspectives using heat disposition factors, fuel cooling effectiveness, and the cooling capacity of the remaining fuel.

Table 1
Evaluation indices of the FTMS. The employed abbreviations are defined in the main text.

Index	Governing equation	Significance
F	$\frac{W_{\mathrm{pro}}}{V_{\mathrm{aircraft}}}$	Amount of available energy
SFC	$\frac{m_{\mathrm{fuel,b}}}{F}$	Total economy of the VCE
ξ_{burn}	$\frac{Q_{\mathrm{burn}}}{Q_{\mathrm{load}}}$	Proportion of heat dissipation by burning
ξ_{ram}	$\frac{Q_{\mathrm{ram}}}{Q_{\mathrm{load}}}$	Proportion of heat dissipation by ram air
ξ_{byp}	$\frac{Q_{\mathrm{byp}}}{Q_{\mathrm{load}}}$	Proportion of heat dissipation by bypass air
ξ_{acc}	$\frac{Q_{\mathrm{acc}}}{Q_{\mathrm{load}}}$	Proportion of heat accumulation
R_{EFF}	$\frac{c_p m_{\mathrm{fuel,b}}(T_{\mathrm{fuel,b}} - T_{\mathrm{fuel,in}})}{c_p m_{\mathrm{fuel,tank}}(T_{\mathrm{fuel,limit}} - T_{\mathrm{fuel,in}})}$	Effectiveness of fuel cooling
R_{RES}	$\frac{c_p M_{\mathrm{tank}}(T_{\mathrm{fuel,limit}} - T_{\mathrm{fuel,tank}})}{c_p M_{\mathrm{tank,0}}(T_{\mathrm{fuel,limit}} - T_{\mathrm{fuel,tank,0}})}$	Residual capability of the fuel cooling in the fuel tank

3 Methods

3.1 Multi-level analysis framework

A multi-level analysis framework is proposed to realistically simulate the mass/energy interactions occurring within the aircraft, VCE, and FTMS. The framework features thermodynamic property, component, subsystem, and evaluation levels (Fig. 3).

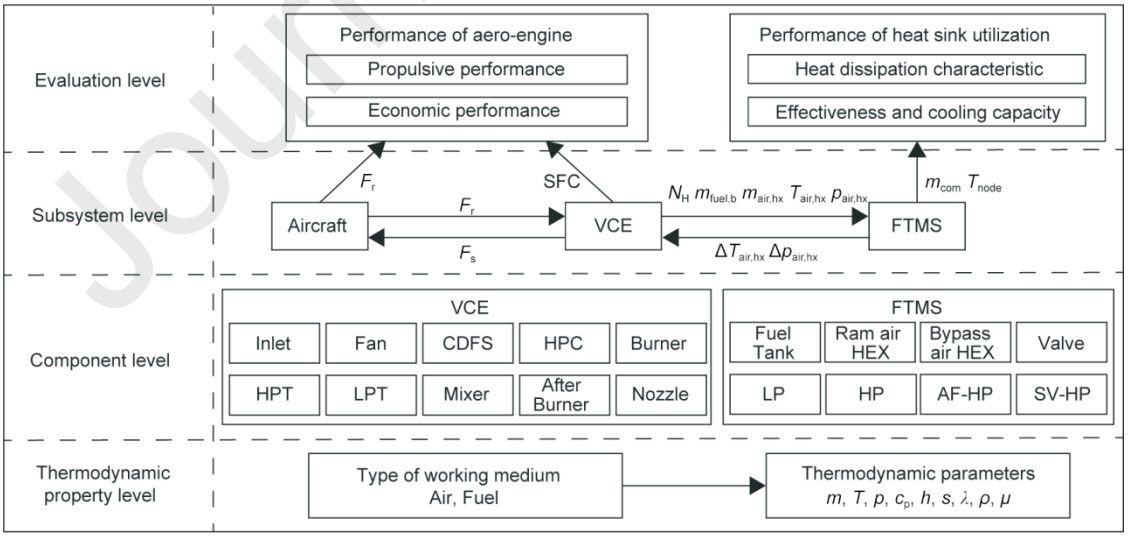

Fig. 3. Schematic of the multi-level analysis framework. The employed abbreviations are defined in the main text and the Nomenclature.

(1) Thermodynamic property level

At the thermodynamic property level, mass flow rate, temperature, and pressure are generally used to describe the basic properties of the working fluid, and other correlative thermodynamic parameters (e.g., specific heat capacity, specific enthalpy, specific entropy, thermal conductivity, and density) can be calculated using empirical relation formulas or data interpolation [36–39].

(2) Component level

T…rnal thermodynamic behavior. When the model is executed, the working fluid parameters at the inlet are assigned as input variables. Subsequently, the component model is operated to determine the working fluid parameters at the outlet. The simulation results can then be effectively utilized at the subsystem level for further analysis and integration. Throughout the modeling process, the thermodynamic properties are precisely calculated at the parameter level.

(3) Subsystem level

The multi-subsystem coupled simulation, which builds upon component-level modeling, aims to describe the interactive processes of mass/energy between the VCE and FTMS by transferring specific thermodynamic parameters. The operating states of the VCE and FTMS depend on the constraints provided by the aircraft performance calculation model.

(4) Evaluation level

Once the subsystem-level calculations are completed, the evaluation criteria mentioned in Table 1 are obtained and used to determine the comprehensive performance of various thermal management schemes at the evaluation level.

3.2 Thermodynamic property-level calculations

At the thermodynamic property level, the thermodynamic properties of the aviation kerosene, fresh air, and combusted gas are considered. The properties of aviation kerosene can be regarded as functions of temperature. The thermodynamic parameters of RP-3, including specific heat capacity, thermal conductivity, density, and dynamic viscosity, have been measured under supercritical pressures within a common temperature range [36–39]. For fresh air and gas, the basic variables are temperature, pressure, and fuel-to-air ratio *f*. The thermodynamic properties of air and gas can be obtained according to the empirical equations in Table 2. a_i and b_i are coefficients of the empirical relationship equations, and the values are obtained from the literature [35].

Table 2
Thermodynamic property model of air and combusted gas. The employed abbreviations are defined in the main text.

Thermodynamic property	Equation
Specific heat capacity	$c_p(T) = c_{p,\mathrm{stan}}(T) + \frac{1+f}{f}\varphi_{c_p}(T), c_{p,\mathrm{stan}}(T) = \sum_{i=1}^{9} a_{i-1}T^{i-1}, \varphi_{c_p}(T) = \sum_{i=1}^{8} b_{i-1}T^{i-1}$ $f = \frac{m_{\mathrm{fuel}}}{m_{\mathrm{air}}}$
Specific enthalpy	$h(T) = \int_{T_{\mathrm{ref}}}^{T} \left[c_{p,\mathrm{stan}}(T) + \frac{1+f}{f}\varphi_{c_p}(T) \right] dT$
Specific entropy	$s(T) = \int \frac{\sum_{i=1}^{9} a_{i-1}T^{i-1} \frac{1+f}{f}\left(\varphi_{c_p}(T) - \varphi_{c_p}(T_{\mathrm{ref}})\right)}{T} dT - R_{\mathrm{g}} ln\left(\frac{p}{p_{\mathrm{ref}}}\right)$

$c_{p,\mathrm{stan}}$ is the standard specific heat capacity of pure air, φ_{cp} is the correction of specific heat capacity of fuel gas, T_{ref} and p_{ref} are the reference temperature and pressure, and their values can be set to 288.15 K and 101.325 kPa, respectively.

3.3 Component-level equations

This section presents the component models in the VCE and FTMS, which can be used at the subsystem simulation level. Table 3 lists the governing equations of each component for the VCE.

Table 3
Governing equations of the variable cycle engine [40]. The employed abbreviations are defined in the main text.

Component	Governing equation
Inlet	Flow through the Inlet is characterized by a constant mass flow rate and specific enthalpy but involves a total pressure loss that is quantified by the pressure recovery coefficient σ. $m_{\mathrm{out}} = m_{\mathrm{in}};\ p_{\mathrm{t,out}} = \sigma p_{\mathrm{t,in}};\ h_{\mathrm{t,out}} = h_{\mathrm{t,in}}$
Fan	At the design point, the pressure ratio π_{Fan} and efficiency η_{Fan} serve as input variables, and at the off-design point, the pressure ratio and efficiency depend on the relative rotation speed N_{L} and auxiliary line index β_{Fan}. $[\pi_{\mathrm{Fan}}, \eta_{\mathrm{Fan}}] = f(N_{\mathrm{L}}, \beta_{\mathrm{Fan}})$ $m_{\mathrm{out}} = m_{\mathrm{in}};\ p_{\mathrm{t,out}} = \pi_{\mathrm{Fan}} p_{\mathrm{t,in}};\ s_{\mathrm{t,out,id}} = s_{\mathrm{t,in}} + R_{\mathrm{g}} \ln \pi_{\mathrm{Fan}};\ h_{\mathrm{t,out}} = h_{\mathrm{t,in}} + \frac{h_{\mathrm{t,out,id}} - h_{\mathrm{t,in}}}{\eta_{\mathrm{Fan}}}$
CDFS	At the design point, the pressure ratio π_{CDFS} and efficiency η_{CDFS} serve as input variables, and at the off-design point, the pressure ratio and efficiency depend on the relative rotation speed N_{H}, blade angle θ_{CDFS}, and auxiliary line index β_{CDFS}. $[\pi_{\mathrm{CDFS}}, \eta_{\mathrm{CDFS}}] = f(N_{\mathrm{H}}, \beta_{\mathrm{CDFS}}, \theta_{\mathrm{CDFS}})$ $m_{\mathrm{out}} = m_{\mathrm{in}};\ p_{\mathrm{t,out}} = \pi_{\mathrm{CDFS}} p_{\mathrm{t,in}};\ s_{\mathrm{t,out,id}} = s_{\mathrm{t,in}} + R_{\mathrm{g}} \ln \pi_{\mathrm{CDFS}};\ h_{\mathrm{t,out}} = h_{\mathrm{t,in}} + \frac{h_{\mathrm{t,out,id}} - h_{\mathrm{t,in}}}{\eta_{\mathrm{CDFS}}}$
Mixer1	In Mixer1, the core air and bypass air mix thoroughly, a process governed by the mass, energy, and momentum conservation equations. $m_{\mathrm{out}} = m_{\mathrm{in},1} + m_{\mathrm{in},2};\ m_{\mathrm{out}} h_{\mathrm{t,out}} = m_{\mathrm{in},1} h_{\mathrm{t,in},1} + m_{\mathrm{in},2} h_{\mathrm{t,in},2};$ $p_{\mathrm{t,out}} f(Ma_{\mathrm{out}}) A_{\mathrm{out}} = p_{\mathrm{t,in},1} f(Ma_{\mathrm{in},1}) A_{\mathrm{in},1} + p_{\mathrm{t,in},2} f(Ma_{\mathrm{in},2}) A_{\mathrm{in},2}$
HPC	The calculation of the characteristic is similar to that of Fan. Considering the inter-stage bleed air, the compression process is divided into two parts, with the pressure ratios before and after the bleeding process denoted as $\pi_{\mathrm{HPC},1}$, and the other one is $\pi_{\mathrm{HPC},2}$, respectively. $m_{\mathrm{in}} = m_{\mathrm{out},1} + \sum m_{\mathrm{ble},1};\ p_{\mathrm{t,out},1} = \pi_{\mathrm{HPC},1} p_{\mathrm{t,in}};$ $s_{\mathrm{t,out,1id}} = s_{\mathrm{t,in}} + R_g \ln \pi_{\mathrm{HPC},1};\ h_{\mathrm{t,out},1} = h_{\mathrm{t,in}} + \frac{h_{\mathrm{t,out,1id}} - h_{\mathrm{t,in}}}{\eta_{\mathrm{HPC}}}$ $m_{\mathrm{out},1} = m_{\mathrm{out},2} + \sum m_{\mathrm{ble},2}; p_{\mathrm{t,out},2} = \pi_{\mathrm{HPC},2} p_{\mathrm{t,out},1};$

Component	Governing equation
	η_{HPC}
Burner	Combustion is initiated in the Burner after the fuel is thoroughly mixed with the compressed airflow. $m_{\mathrm{out}} = m_{\mathrm{in}} + m_{\mathrm{fuel}};\ p_{\mathrm{t,out}} = \sigma_{\mathrm{b}} p_{\mathrm{t,in}};\ m_{\mathrm{in}} h_{\mathrm{t,in}} + \eta_{\mathrm{b}} m_{\mathrm{fuel}} \mathrm{LHV} = m_{\mathrm{out}} h_{\mathrm{t,out}}$ where σ_{b} is the pressure recovery coefficient of the Burner.
HPT	The HPT model incorporates three sequential thermodynamic processes: isobaric blending of combustion gas and cooling air, adiabatic expansion, and rotor blending. HPT stator blending: $m_{\mathrm{out},1} = m_{\mathrm{in},1} + m_{\mathrm{in},2};\ p_{\mathrm{t,out},1} = p_{\mathrm{t,in},1};\ m_{\mathrm{out},1} h_{\mathrm{t,out},1} = m_{\mathrm{in},1} h_{\mathrm{t,in},1} + m_{\mathrm{in},2} h_{\mathrm{t,in},2}$ HPT rotor expansion: $m_{\mathrm{out},2} = m_{\mathrm{out},1};\ h_{\mathrm{t,out},2} = h_{\mathrm{t,out},1} - \eta_{\mathrm{HPT}}(h_{\mathrm{t,out},1} - h_{\mathrm{t,out,2id}});$ $p_{\mathrm{t,out},2} = \frac{p_{\mathrm{t,out},1}}{\pi_{\mathrm{HPT}}};\ s_{\mathrm{t,out,2id}} = s_{\mathrm{t,out},1} + R_{\mathrm{g}} \ln(\pi_{\mathrm{HPT}})$ HPT rotor blending: $m_{\mathrm{out},3} = m_{\mathrm{out},2} + m_{\mathrm{in},3};\ p_{\mathrm{t,out},3} = p_{\mathrm{t,out},2};\ m_{\mathrm{out},3} h_{\mathrm{t,out},3} = m_{\mathrm{out},2} h_{\mathrm{t,out},2} + m_{\mathrm{in},3} h_{\mathrm{t,in},3}$
LPT	The calculation of the characteristic is similar to that of HPT.
Mixer2	The calculation of the characteristic is similar to that of Mixer1.
AF-Burner	The calculation of the characteristic is similar to that of Burner.
Nozzle	The Nozzle outlet pressure depends on the relative magnitude of the critical pressure p_{cri} and environmental pressure p_{e}. $m_{\mathrm{out}} = m_{\mathrm{in}};\ h_{\mathrm{t,out}} = h_{\mathrm{t,in}};$ $p_{\mathrm{out}} = \begin{cases} p_{\mathrm{e}}, p_{\mathrm{cri}} < p_{\mathrm{e}} \\ p_{\mathrm{cri}}, p_{\mathrm{cri}} \geq p_{\mathrm{e}} \end{cases}, p_{\mathrm{cri}} = p_{\mathrm{t,out}} \left(1 + \frac{A_9}{A_8} \frac{k-1}{2}\right)^{\frac{k}{k-1}}$ where k is the specific heat ratio.

According to the operating principles, the FTMS components can be classified as tanks, pumps, valves, and heat exchangers.

● **Tank.** Due to the substantial fuel reserves in the tank, the heat capacity of the fuel and tank itself should be considered at each time step. Within the tank, the fuel mass flow rate is dictated by the FTMS requirements, whereas the fuel pressure depends on the storage conditions.

Input parameters: [m_{in}, m_{out}, T_{in}, T_{e}, p_{in}].

Output parameters: [M_{fuel}, T_{fuel}, T_{tank}, p_{out}].

Control parameters: [$M_{\mathrm{fuel,max}}$, A_{tank}, p_{tank}].

Continuity equation:

$$\frac{\mathrm{d}M_{\mathrm{fuel}}}{\mathrm{d}t} = m_{\mathrm{in}} - m_{\mathrm{out}} \quad (14)$$

Pressure balance equation:

$$p_{\mathrm{out}} = p_{\mathrm{in}} = p_{\mathrm{tank}} \quad (15)$$

where p_{tank} is the pressure in the tank.

Energy conservation equations [41]:

For the fuel:

$$Q_{\mathrm{inner}} + m_{\mathrm{in}} h_{\mathrm{in}} - m_{\mathrm{out}} h_{\mathrm{out}} = \frac{\mathrm{d}E_{\mathrm{fuel}}}{\mathrm{d}t} \quad (16)$$

For the tank:

$$Q_{\mathrm{outer}} - Q_{\mathrm{inner}} = \frac{\mathrm{d}E_{\mathrm{fuel}}}{\mathrm{d}t} \quad (17)$$

Q_{inner} and Q_{outer} are calculated as

$$Q_{\mathrm{inner}} = \alpha_{\mathrm{inner}} A_{\mathrm{tank}} (T_{\mathrm{tank}} - T_{\mathrm{fuel}}) \quad (18)$$

$$Q_{\mathrm{outer}} = \alpha_{\mathrm{outer}} A_{\mathrm{tank}} (T_{\mathrm{aw}} - T_{\mathrm{tank}}) \quad (19)$$

where α_{inner} and α_{outer} refer to the coefficients for convective heat transfer inside and outside the tank, respectively; T_{aw} is the adiabatic wall temperature outside the tank; A_{tank} is the heat exchange area of the tank, determined from the tank capacity ($M_{\mathrm{fuel,max}}$):

$$A_{\mathrm{tank}} = 6\left(\frac{M_{\mathrm{fuel,max}}}{\rho}\right)^{\frac{2}{3}} \quad (20)$$

The heat exchange between the in-tank fuel and tank walls can be regarded as a natural convection-based heat transfer within a confined space and is modeled as follows [42]:

$$Nu_{\mathrm{inner}} = \begin{cases} 0.212(Gr \cdot Pr)^{0.25} 10^4 \leq Gr \leq 4.6 \times 10^5 \\ 0.061(Gr \cdot Pr)^{0.33} Gr > 4.6 \times 10^5 \end{cases} \quad (21)$$

T_{aw} can be determined from the environmental temperature T_{e} and velocity V_{aircraft} as follows:

$$T_{\mathrm{aw}} = T_{\mathrm{e}} + r\frac{V_{\mathrm{aircraft}}^2}{2c_p} \quad (22)$$

where r is the recovery factor.

The heat exchange process between the tank wall and external airflow can be approximated as the heat transfer for the airflow over a flat plate [42]:

N $\begin{cases} 0.664Re^{0.5}Pr^{0.33} & Re < 5\times10^5 \end{cases}$

The reference temperature T_{ref} can be expressed as

$$T_{\mathrm{ref}} = T_{\mathrm{e}} + 0.5(T_{\mathrm{tank}} - T_{\mathrm{e}}) + 0.22(T_{\mathrm{aw}} - T_{\mathrm{e}}) \quad (24)$$

● **Pump.** Considering the pump, since the input power cannot be fully converted into the pressure potential energy of the fuel during operation, the power loss is dissipated into the fuel as thermal energy. The error in calculating the temperature rise of the fluid based on the pump efficiency did not exceed 3% [43].

Input parameters: [m_{in}, T_{in}, p_{in}].

Output parameters: [m_{out}, T_{out}, p_{out}].

Control parameters: [N_{H}, η_{p}, Δp].

Continuity equation:

$$m_{\mathrm{out}} = m_{\mathrm{in}} \quad (25)$$

Pressure balance equation:

$$p_{\mathrm{out}} = p_{\mathrm{in}} + \Delta p \quad (26)$$

where η_{p} and Δp represent the efficiency and pressure rise of the fluid, respectively, and can be determined from N_{H} and m_{in}:

$$[\eta_{\mathrm{p}}, \Delta p] = f(N_{\mathrm{H}}, m_{\mathrm{in}}) \quad (27)$$

Energy conservation equations [43]:

For the fuel:

$$Q_{\mathrm{pump}} + \eta_{\mathrm{p}} W_p + m_{\mathrm{in}} h_{\mathrm{in}} - m_{\mathrm{out}} h_{\mathrm{out}} = \frac{dE_{\mathrm{fuel}}}{dt} \quad (28)$$

$$W_p = \frac{m_{\mathrm{in}} \Delta p}{\eta_{\mathrm{p}} \rho} \quad (29)$$

$$Q_{\mathrm{pump}} = (1 - \eta_{\mathrm{p}}) W_{\mathrm{p}} \quad (30)$$

● **Valve.** When the fuel passes through a valve, a pressure drop occurs because of the fuel viscosity, and the pressure potential energy is converted into thermal energy.

Input parameters: [m_{in}, T_{in}, p_{in}].

Output parameters: [m_{out}, T_{out}, p_{out}].

Control parameter: [Δp].

Continuity equation:

$$m_{\mathrm{out}} = m_{\mathrm{in}} \quad (31)$$

Pressure balance equation:

$$p_{\mathrm{out}} = p_{\mathrm{in}} - \Delta p \quad (32)$$

Δp is dependent on the pressure distribution of the FTMS and can be calculated by accounting for processes such as the pressure rise provided by pumps and pressure drops across heat exchangers.

Energy conservation equations [44]:

For the fuel:

$$Q_{\mathrm{loss}} + m_{\mathrm{in}} h_{\mathrm{in}} - m_{\mathrm{out}} h_{\mathrm{out}} = \frac{dE_{\mathrm{fuel}}}{dt} \quad (33)$$

$$Q_{\mathrm{loss}} = \frac{m_{\mathrm{in}} \Delta p}{\rho} \quad (34)$$

● **Heat exchanger.** In the conventional heat exchanger design, the law of energy conservation is commonly employed to calculate the changes of the working fluid temperature. However, this approach exhibits limitations in its applicability to performance evaluation under complex flight missions owing to the substantial variability in heat transfer efficiency. Hence, adjusting the heat transfer characteristics of heat exchangers to accommodate varying operation conditions becomes particularly necessary [45].

Input parameters: [$m_{\mathrm{h,in}}$, $T_{\mathrm{h,in}}$, $p_{\mathrm{h,in}}$, $m_{\mathrm{c,in}}$, $T_{\mathrm{c,in}}$, $p_{\mathrm{c,in}}$].

Output parameters: [$m_{\mathrm{h,out}}$, $T_{\mathrm{h,out}}$, $p_{\mathrm{h,out}}$, $m_{\mathrm{c,out}}$, $T_{\mathrm{c,out}}$, $p_{\mathrm{c,out}}$].

Control parameters: [$K_{\mathrm{des,h}}$, A_{h}, $A_{\mathrm{f,h}}$, ε_{h}, A_{c}, $A_{\mathrm{f,c}}$, ε_{c}].

Continuity equations:

$$m_{\mathrm{h,out}} = m_{\mathrm{h,in}} \quad (35)$$

$$m_{\mathrm{c,out}} = m_{\mathrm{c,in}} \quad (36)$$

Pressure balance equations:

$$p_{\mathrm{h,out}} = (1 - \varepsilon_{\mathrm{h}}) p_{\mathrm{h,in}} \quad (37)$$

$$p_{\mathrm{c,out}} = (1 - \varepsilon_{\mathrm{c}}) p_{\mathrm{c,in}} \quad (38)$$

where ε_{h} and ε_{c} represent the resistance coefficients of the hot and cold fluids, respectively.

The heat transfer rate at the design point is given by

$$Q_{\mathrm{des}} = \eta_{\mathrm{des}} \min(c_{p,\mathrm{h}} m_{\mathrm{des,h}}, c_{p,c} m_{\mathrm{des,c}}) (T_{\mathrm{h,in}} - T_{\mathrm{c,in}}) \quad (39)$$

where η_{des} is the heat transfer effectiveness.

For common heat exchanger arrangements, namely parallel-flow and counter-flow, $\eta_{\mathrm{des,pa}}$ and $\eta_{\mathrm{des,co}}$ are defined by the following equations:

$$\eta_{\mathrm{des,pa}} = \frac{1 - \exp[-\mathrm{NTU}(1+R)]}{1+R} \quad (40)$$

$$\eta_{\mathrm{des,co}} = \frac{1 - \exp[-\mathrm{NTU}(1-R)]}{1 - R\exp[-\mathrm{NTU}(1-R)]} \quad (41)$$

where NTU and R are the number of transfer units and the ratio of the heat capacity, respectively, and can be determined as

$$\mathrm{NTU}=\frac{K_{\mathrm{des,h}}A_{\mathrm{h}}}{\min(c_{p,\mathrm{h}}m_{\mathrm{des,h}},c_{p,c}m_{\mathrm{des,c}})}\quad(43)$$

where $K_{\mathrm{des,h}}$ and A_{h} are the heat transfer coefficient and heat transfer area of the hot side, respectively.

However, multi-pass cross-flow heat exchangers are prevalent in aeroengines. For a single segment, the heat transfer effectiveness η_{sig} is defined as [46]

$$\eta_{\mathrm{sig}}=\frac{1-\exp\{-R[1-\exp(-\mathrm{NTU}_{\mathrm{sig}})]\}}{R}\quad(44)$$

For an n-segment heat exchanger, the overall heat transfer effectiveness $\eta_{\mathrm{des,cro}}$ of multi-pass cross-flow heat exchangers is formally defined as

$$\left(\frac{1-\eta_{\mathrm{des,cro}}}{1-\eta_{\mathrm{des,cro}}R}\right)=\left(\frac{1-\eta_{\mathrm{sig}}}{1-\eta_{\mathrm{sig}}R}\right)^{n}\quad(45)$$

$$\mathrm{NTU}=n\mathrm{NTU}_{\mathrm{sig}}\quad(46)$$

The heat transfer coefficient of the hot side at the off-design point $K_{\mathrm{off,h}}$ can be derived from the design-point condition to determine the heat transfer rates under different working conditions. C_{h}, C_{c}, x_{h}, x_{c}, y_{h}, and y_{c} are introduced to quantify the numerical correlations between Nu, Re, and Pr on the hot and cold sides of the heat exchanger.

$$K_{\mathrm{off,h}}=K_{\mathrm{des,h}}\frac{\frac{1}{C_{\mathrm{h}}d_{\mathrm{h}}^{x_{\mathrm{h}}-1}A_{\mathrm{f,h}}^{-x_{\mathrm{h}}}A_{\mathrm{h}}m_{\mathrm{des,h}}^{x_{\mathrm{h}}}c_{p,\mathrm{des,h}}^{y_{\mathrm{h}}}\mu_{\mathrm{des,h}}^{y_{\mathrm{h}}-x_{\mathrm{h}}}\lambda_{\mathrm{des,h}}^{1-y_{\mathrm{h}}}}+\frac{1}{C_{c}d_{c}^{x_{\mathrm{c}}-1}A_{\mathrm{f,c}}^{-x_{\mathrm{c}}}A_{\mathrm{c}}m_{\mathrm{des,c}}^{x_{\mathrm{c}}}c_{p,\mathrm{des,c}}^{y_{\mathrm{c}}}\mu_{\mathrm{des,c}}^{y_{\mathrm{c}}-x_{\mathrm{c}}}\lambda_{\mathrm{des,c}}^{1-y_{\mathrm{c}}}}}{\frac{1}{C_{\mathrm{h}}d_{\mathrm{h}}^{x_{\mathrm{h}}-1}A_{\mathrm{f,h}}^{-x_{\mathrm{h}}}A_{\mathrm{h}}m_{\mathrm{off,h}}^{x_{\mathrm{h}}}c_{p,\mathrm{off,h}}^{y_{\mathrm{h}}}\mu_{\mathrm{off,h}}^{y_{\mathrm{h}}-x_{\mathrm{h}}}\lambda_{\mathrm{off,h}}^{1-y_{\mathrm{h}}}}+\frac{1}{C_{c}d_{c}^{x_{\mathrm{c}}-1}A_{f,c}^{-x_{\mathrm{c}}}A_{\mathrm{c}}m_{\mathrm{off,c}}^{x_{\mathrm{c}}}c_{p,\mathrm{off,c}}^{y_{\mathrm{c}}}\mu_{\mathrm{off,c}}^{y_{\mathrm{c}}-x_{\mathrm{c}}}\lambda_{\mathrm{off,c}}^{1-y_{\mathrm{c}}}}}\quad(47)$$

$$Nu_{\mathrm{off,h}}=C_{\mathrm{h}}Re^{x_{\mathrm{h}}}Pr^{y_{\mathrm{h}}}\quad(48)$$

$$Nu_{\mathrm{off,c}}=C_{\mathrm{c}}Re^{x_{\mathrm{c}}}Pr^{y_{\mathrm{c}}}\quad(49)$$

where $K_{\mathrm{off,h}}$ denotes the heat transfer coefficient at the off-design point; d is the hydraulic diameter; A_{f} is the flow area; C is the empirical constant; x and y represent the exponents of Re and Pr, respectively.

3.4 Subsystem-level models

The integrated simulation framework comprises three subsystem-level models: aircraft, VCE, and FTMS. Performance analysis of these subsystems provides the requisite boundary conditions for the integrated system simulation.

- **Aircraft.** The aircraft performance evaluation model serves to solve the required thrust and lift-drag characteristics of the aircraft in different flight missions, thereby providing boundary parameters for the VCE performance analysis.

Input parameters: [H, Ma, ΔH, ΔV, Δt].

Output parameter: F_{r}.

Control parameters: [M, A, DI].

The assumptions made for aircraft modeling herein are as follows:

(1) The takeoff weight of the aircraft is set to 25000 kg and assumed to progressively decrease throughout the mission because of fuel consumption.

(2) The aircraft maintains a constant acceleration or climbing rate during a specific mission segment.

The calculation flowchart of the aircraft performance model is illustrated in Fig. 4.

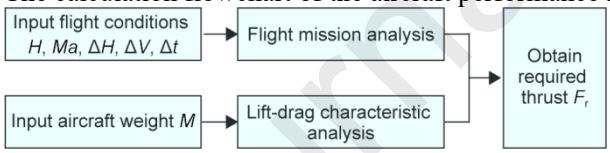

Fig. 4. Calculation flowchart of the aircraft performance model. The employed abbreviations are defined in the main text.

The required thrust F_{r} is determined by the flight conditions and weight M [47]:

$$F_{\mathrm{r}}=\frac{Mg}{V}\frac{\mathrm{d}}{\mathrm{d}t}\left(H+\frac{V^2}{2g}\right)+D\quad(50)$$

The flight drag D is equivalent to

$$D=qAC_D\quad(51)$$

where q is the dynamic pressure, A is the windward area of the wings, and C_D is the drag coefficient, which is given by

$$C_D=C_{D,\min}DI+\varepsilon(C_L-C_{LD,\min})^2,C_L=\frac{n_{\mathrm{o}}Wg}{qA}\quad(52)$$

where $C_{D,\min}$ is the minimum drag coefficient determined by the aircraft's windward area and aerodynamic layout; DI is the external store drag coefficient, which is set to one in this study, as no external stores are considered; ε is the resistance coefficient determined by the flight state; C_L is the lift coefficient; $C_{LD,\min}$ is the lift coefficient corresponding to $C_{D,\min}$, and n_{o} is the overload factor.

The equation for calculating F_{r} can be simplified under different flight missions, as shown in Table 4 [48]:

Table 4

Required thrust under different flight missions [48]. The employed abbreviations are defined in the main text.

Mission	Required thrust
Takeoff	$F_{\mathrm{r}}=\frac{V_{\mathrm{to}}^2}{2d}M+D$
Acceleration	$F_{\mathrm{r}}=\frac{\Delta V}{\Delta t}M+D$

Climb	$\frac{\Delta H}{V_{to}} = \frac{Mg}{2}$
Cruise	$F_r = D$

V_{to} is the takeoff speed of the aircraft.

- **VCE.** The VCE model is a thermodynamic cycle simulation used to determine engine performance and thermodynamic parameters at the principal sections, furnishing the FTMS with essential boundary parameters and supporting system-level performance evaluations.

Input parameters: [H, Ma].

Output parameters: [F, SFC].

Control parameter: N_H.

The assumptions made for VCE modeling herein are listed as follows:

(1) The flow within the engine is considered one-dimensional and steady.

(2) The air or combustion gas within the engine is an ideal gas obeying the ideal gas equation.

(3) The specific heat capacity at constant pressure c_p and specific heat ratio k are constant within each major component (Inlet, Fan, CDFS, HPT, etc.), but vary from one component to another.

(4) The effects of the inlet distortion and tip leakage on the overall engine performance are negligible.

The calculation flowchart of the VCE performance model is shown in Fig. 5.

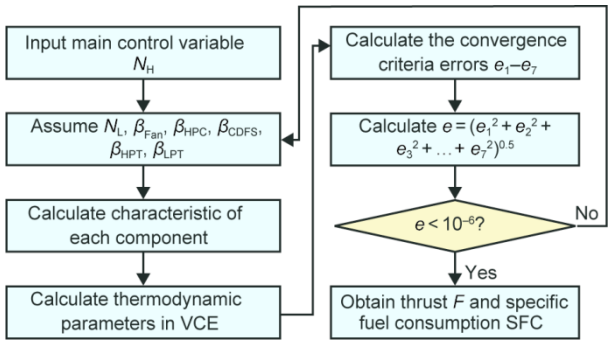

Fig. 5. Calculation flowchart of the VCE performance model. The employed abbreviations are defined in the main text.

(1) The VCE performance analysis regards the relative rotation speed of the high-pressure shaft N_H as the main control variable and assumes the relative rotation speed of the low-pressure shaft N_L and auxiliary line indices of Fan, HPC, CDFS, HPT, and LPT (β_{Fan}, β_{HPC}, β_{CDFS}, β_{HPT}, and β_{LPT}) as calculation conditions.

(2) With the cycle parameters defined, the component performance is calculated sequentially from Inlet to Nozzle, based on the equations listed in Table 3, to obtain the thermodynamic parameters in the VCE.

(3) The VCE performance calculation involves solving a nonlinear multi-equation process, and the convergence principle is as follows:

- The power delivered by the HPT (W_{HPT}) must balance the power consumed by HPC and CDFS.
- The power delivered by the LPT (W_{LPT}) must balance the power consumed by the Fan.

The model-calculated HPT inlet flow rate ($m_{HPT,model}$) must match the value interpolated from the component characteristic map ($m_{HPT,line}$).

The model-calculated LPT inlet flow rate ($m_{LPT,model}$) must match the value interpolated from the component characteristic map ($m_{LPT,line}$).

- The static pressure at the exit of the inner bypass duct ($p_{out,byp1}$) is equal to that at the exit of the secondary bypass duct ($p_{out,byp2}$).
- The static pressure at the exit of the bypass duct ($p_{out,byp}$) is equal to that at the exit of the core engine ($p_{out,core}$).
- The nozzle throat area A_8 is held constant at its design value $A_{8,des}$.

$$\begin{cases} e_1 = \frac{W_{HPT}\eta_{axis,H} - W_{HPC} - W_{CDFS}}{W_{HPC} + W_{CDFS}} = f_1(N_H, N_L, \beta_{Fan}, \beta_{HPC}, \beta_{CDFS}, \beta_{HPT}, \beta_{LPT}) \\ e_2 = \frac{W_{LPT}\eta_{axis,L} - W_{FAN}}{W_{FAN}} = f_2(N_H, N_L, \beta_{Fan}, \beta_{HPC}, \beta_{CDFS}, \beta_{HPT}, \beta_{LPT}) \\ e_3 = \frac{m_{HPT,model} - m_{HPT,line}}{m_{HPT,line}} = f_3(N_H, N_L, \beta_{Fan}, \beta_{HPC}, \beta_{CDFS}, \beta_{HPT}, \beta_{LPT}) \\ e_4 = \frac{m_{LPT,model} - m_{LPT,line}}{m_{LPT,line}} = f_4(N_H, N_L, \beta_{Fan}, \beta_{HPC}, \beta_{CDFS}, \beta_{HPT}, \beta_{LPT}) \\ e_5 = \frac{p_{out,byp1} - p_{out,byp2}}{p_{out,byp2}} = f_5(N_H, N_L, \beta_{Fan}, \beta_{HPC}, \beta_{CDFS}, \beta_{HPT}, \beta_{LPT}) \\ e_6 = \frac{p_{out,byp} - p_{out,core}}{p_{out,core}} = f_6(N_H, N_L, \beta_{Fan}, \beta_{HPC}, \beta_{CDFS}, \beta_{HPT}, \beta_{LPT}) \\ e_7 = \frac{A_8 - A_{8,des}}{A_{8,des}} = f_7(N_H, N_L, \beta_{Fan}, \beta_{HPC}, \beta_{CDFS}, \beta_{HPT}, \beta_{LPT}) \end{cases} \quad (53)$$

where $\eta_{axis,H}$ and $\eta_{axis,L}$ are the efficiencies of the high-pressure shaft and the low-pressure shafts, respectively.

(4) The variables N_L, β_{Fan}, β_{HPC}, β_{CDFS}, β_{HPT}, and β_{LPT} need to be readjusted employing the Newton–Raphson iteration method until all parts of Eq. (53) converge.

- **FTMS.** The FTMS model is developed to characterize the temperature rise of the fuel as it circulates through the multi-branch system, providing data for analyzing the heat dissipation and accumulation characteristics.

Input parameters: [N_H, $m_{fuel,b}$, $m_{air,hx}$, $T_{air,hx}$, $p_{air,hx}$].

Output parameters: [m_{com}, T_{node}, p_{node}]

C

The assumptions made for FTMS modeling herein are listed as follows:

(1) The fuel mass flow rates for HP_{engine} and $AF\text{-}HP_{engine}$ branches are determined by VCE demand, and the mass flow rate of the servo actuation system is assumed to be constant (0.3 $kg \cdot s^{-1}$).

(2) The pump performance is governed by N_H and m_{in}.

(3) The initial mass and temperature of the fuel in the tank are 4000 kg and 313.15 K, respectively.

(4) The maximum allowable fuel temperature is 420 K.

The calculation flowchart of the FTMS performance model is presented in Fig. 6.

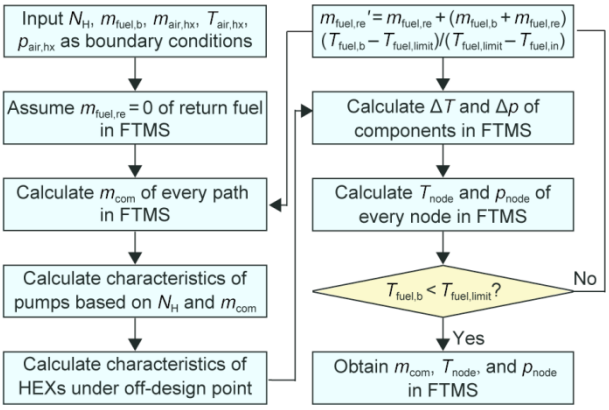

Fig. 6. Calculation flowchart of the FTMS performance model. The employed abbreviations are defined in the main text.

(1) Input N_H, $m_{fuel,b}$, $m_{air,hx}$, $T_{air,hx}$, and $p_{air,hx}$ from the VCE simulation results as boundary conditions of the FTMS performance model.

(2) Assume that the mass flow rate of the return fuel $m_{fuel,re}$ = 0, to establish a flow distribution within the network considering the required mass flow $m_{fuel,b}$ of the VCE.

(3) Calculate the characteristics of the pumps and HEXs. The operating characteristics of the pumps can be obtained from the performance map and N_H, and the heat transfer rates of the $HEX_{fuel–ram\ air}$ and $HEX_{fuel–bypass\ air}$ are calculated by the performance model introduced in Section 3.3.

(4) Conduct performance matching analysis starting from the fuel tank. This process involves the sequential application of component-level models to determine the temperature and pressure at each node in the FTMS network.

(5) Determine $m_{fuel,re}$ that satisfies the thermal constraints of the system. As $T_{fuel,b}$ is the point of highest temperature within the FTMS, it is compared with the maximum allowable temperature $T_{fuel,limit}$ to decide if the return fuel valve should be opened to increase the total fuel flow. A constraint violation triggers an iterative correction of $m_{fuel,re}$ that is systematically adjusted based on the discrepancy between the actual and maximum theoretical heat absorptions:

$$m_{fuel,re}' = m_{fuel,re} + (m_{fuel,b} + m_{fuel,re})\frac{T_{fuel,b} - T_{fuel,limit}}{T_{fuel,limit} - T_{fuel,in}} \quad (54)$$

3.5 Integrated simulation process

In the coupled system, heat transfer, transport, and conversion occur among different subsystems and components; thus, the analysis of this coupled system fundamentally relies on ensuring the consistent exchange and matching of data at the interfaces between multiple subsystems [45]. The calculation process of the analysis is illustrated in Fig. 7.

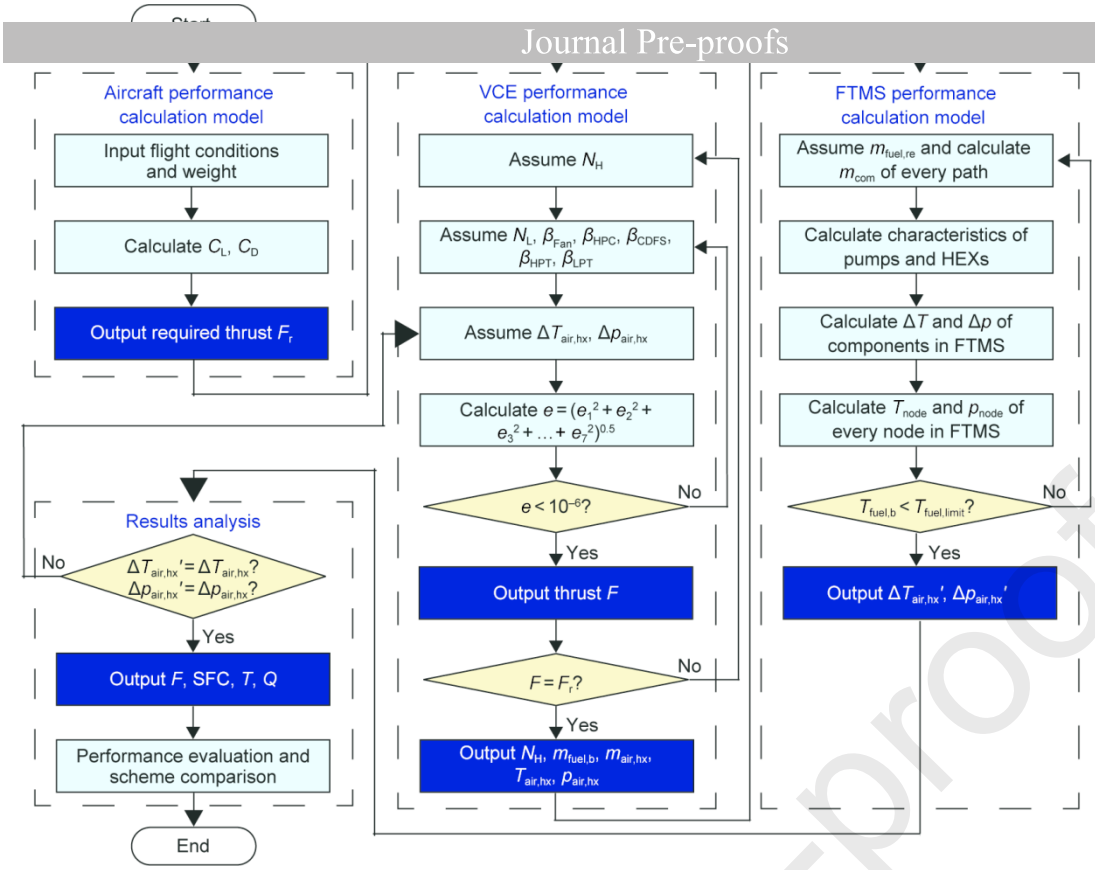

Fig. 7. Calculation process of VCE and FTMS analysis. The employed abbreviations are defined in the main text.

(1) Input flight conditions and weight to describe the working condition of the aircraft.

(2) Transfer the required thrust F_r to the VCE model. F_r can be determined based on the flight mission, lift-drag characteristics of the aircraft, and weight considering the fuel consumption since the start of the mission.

(3) Calculate the thermodynamic performance of the VCE. Choose N_H as the main control variable, then select N_L, β_{Fan}, β_{HPC}, β_{CDFS}, β_{HPT}, and β_{LPT} as independent variables to obtain VCE performance via the method described in Section 3.4. During this solution process, the impact of the $HEX_{fuel-bypass\ air}$ on the engine must be considered. Therefore, it is also necessary to assume the temperature and pressure changes of the secondary bypass air ($\Delta T_{air,hx}'$, $\Delta p_{air,hx}'$) as it flows across $HEX_{fuel-bypass\ air}$.

(4) Match the working conditions of the VCE to meet the thrust requirement. Evaluate the residual between the calculated thrust F of the VCE and required thrust F_r. If the residual exceeds the convergence tolerance, N_H is updated via the following equation, and the calculation process reverts to Step (3):

$$N_H' = \left(\frac{F_r}{F}\right)^{0.15} N_H \quad (55)$$

(5) Transfer the rotational speed N_H, mass flow rate of the fuel for burning $m_{fuel,b}$, and thermodynamic parameters of the secondary bypass air ($m_{air,hx}$, $p_{air,hx}$, $T_{air,hx}$) at the inlet of the $HEX_{fuel-bypass\ air}$ to the FTMS.

(6) Calculate the thermal performance of the FTMS. Utilizing the boundary parameters transferred from the VCE and assuming the mass flow rate of the return fuel $m_{fuel,re}$, we can determine the operating characteristics of each component in the FTMS, as well as the thermodynamic parameters of each flow path. By evaluating whether the fuel temperature in front of the burner complies with the preset threshold, we can rationally adjust $m_{fuel,re}$ to calibrate the temperature and mass-flow distribution in the FTMS.

(7) Examine the output values ($\Delta T_{air,hx}$, $\Delta p_{air,hx}$) of the FTMS performance calculation model. If they are inconsistent with the values assumed in Step (3), the VCE and FTMS models have yielded different solutions for the parameter changes in the secondary bypass air. Consequently, the newly generated outputs should be applied as boundary conditions for the VCE simulation, and the entire process should return to Step (3) for recalculation.

(8) Evaluate the performance of the VCE and FTMS, including F, SFC of the VCE, as well as the heat dissipation and accumulation of the FTMS, to support comprehensive comparisons of different thermal management strategies.

3.6 Method validation

The foregoing analysis provides a solid foundation for the coupled simulation model. The fidelity of this model directly determines the credibility of the subsequent analysis of the advantages of the heat sink and different schemes. The coupled simulation model is conducted at the component and subsystem levels. Regarding the simulation tools, the VCE and FTMS models are validated using the GasTurb and AMESim programs, respectively.

Fig. 8 presents the simulation validation results obtained for the representative components of the VCE (HPC, HPT, and Burner) and FTMS (HP_{engine}, $Valve_{sv}$, and $HEX_{fuel-bypass\ air}$) models under the sea level static (SLS) condition. Compared with

the calculation results of commercial software, the simulation results exhibit an average error of < 1% and a maximum error of 1

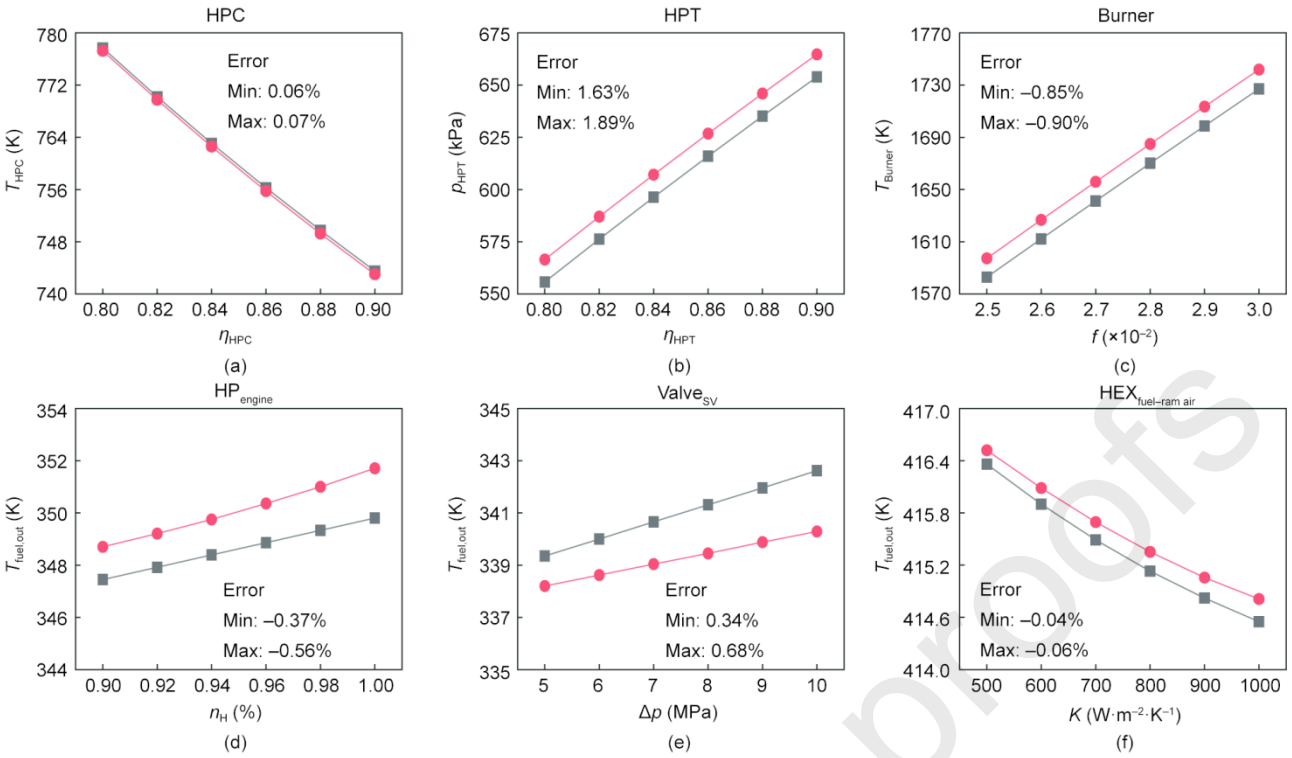

Fig. 8. Validation results obtained for different components. The employed abbreviations are defined in the main text. (a) Outlet temperature of HPC; (b) outlet pressure of HPT; (c) outlet temperature of Burner; (d) outlet temperature of HP_{engine}; (e) outlet temperature of $Valve_{sv}$; (f) outlet temperature of $HEX_{fuel–ram\ air}$.

Two working conditions (SLS and subsonic cruise conditions) are selected based on the cycle parameters from reference results [40]. Table 5 and Table 6 compare the key parameters of the proposed model with those of the commercial software (GasTurb).

Table 5
Validation of the VCE model: sea level static condition. The employed abbreviations are defined in the main text.

Parameter	SLS condition (H = 0 km, Ma = 0)				
	Model	GasTurb	Error (vs GasTurb, %)	Literature [40]	Error (vs literature %)
F (kN)	85.04	82.08	3.61	84.53	0.60
SFC (kg·N^{-1}·h^{-1})	0.0754	0.0744	1.34	0.0723	4.29
T_{HPC} (K)	756.26	755.75	0.07	762.03	−0.76
p_{HPC} (kPa)	2063.99	2063.99	< 0.01	2105.32	−1.96
T_{Nozzle} (K)	838.15	836.71	0.17	820.41	2.16
P_{Nozzle} (kPa)	295.85	299.96	−1.37	300.27	−1.47
$m_{fuel,b}$ (kg·s^{-1})	1.78	1.70	4.71	—	—
$m_{air,hx}$ (kg·s^{-1})	36.00	34.92	3.09	—	—
$T_{air,hx}$ (K)	412.73	412.58	0.04	—	—
$p_{air,hx}$ (kPa)	294.86	294.86	< 0.01	—	—

Table 6
Validation of the VCE model: subsonic cruise. The employed abbreviations are defined in the main text.

Parameter	Subsonic cruise (H = 11 km, Ma = 0.8)				
	Model	GasTurb	Error (vs GasTurb, %)	Literature [40]	Error (vs literature, %)
F (kN)	27.97	26.79	4.40	27.28	2.53
SFC (kg·N^{-1}·h^{-1})	0.0983	0.0982	0.10	0.0950	3.47
T_{HPC} (K)	732.25	730.14	0.29	732.62	−0.05
p_{HPC} (kPa)	860.87	864.47	−0.42	866.42	−0.64
T_{Nozzle} (K)	838.71	842.18	−0.41	819.60	2.33
P_{Nozzle} (kPa)	117.62	119.20	−1.33	118.19	−0.48
$m_{fuel,b}$ (kg·s^{-1})	0.76	0.73	4.11	—	—
$m_{air,hx}$ (kg·s^{-1})	12.49	11.90	4.96	—	—
$T_{air,hx}$ (K)	386.40	383.93	0.64	—	—
$p_{air,hx}$ (kPa)	114.52	113.82	0.62	—	—

Based on the FTMS architecture shown in Fig. 1, a simulation model is constructed in AMESim, and its simulation accuracy is assessed for key performance parameters, such as $\Delta T_{air,hx}$, $\Delta p_{air,hx}$, and thermodynamic parameters at critical system nodes. The calculation method for the flow rate and temperature of the ram air is adopted from the literature [49] and the heat loads within the FTMS for different phases presented in Table 7. Specifically, Q_{hyd} and Q_{avi} are based on data from the literature [50]. A representative heat load of 50 kW is assumed for Q_{ecs} across the flight envelope, while Q_{oil} is set to 50 kW for supersonic cruise [51] and 25 kW for other conditions.

For the validation case, $HEX_{fuel–ram\ air}$ and $HEX_{fuel–bypass\ air}$ are configured with identical heat transfer areas and a four-segment cross-flow structure. The effectiveness of $HEX_{fuel–bypass\ air}$ can be determined using the methodology in Section 3.3

based on the specified parameters for $HEX_{fuel-ram\ air}$ (heat transfer coefficient = 200 $W \cdot m^{-2} \cdot K^{-1}$, heat transfer area = 0.5 m^2). In a

Table 7
Heat loads within the FTMS for different phases [50]. The employed abbreviations are defined in the main text.

Operating Condition	Q_{ecs} (kW)	Q_{hyd} (kW)	Q_{avi} (kW)	Q_{oil} (kW)
Ground idle	50	27.11	10.59	25
Cruise	50	29.24	10.90	25
Supersonic	50	35.22	12.31	50
Loiter	50	30.81	8.62	25

The results of the aforementioned simulations of the VCE and FTMS are benchmarked against those obtained using commercial software. An average error of < 2% and a maximum error of 5.41% obtained for the key parameters demonstrate the reliability of the proposed coupled modeling approach and component-level equations.

Table 8
Validation results of the FTMS model. The employed abbreviations are defined in the main text.

Parameters	SLS condition (H = 0 km, Ma = 0, N_H = 100%)			Subsonic cruise (H = 11 km, Ma = 0.8, N_H = 80%)		
	Model	AMESim	Error (%)	Model	AMESim	Error (%)
$m_{fuel,re}$ ($kg \cdot s^{-1}$)	0	0	—	0.39	0.37	5.41
$\Delta p_{air,hx}$ (kPa)	4.05	4.05	0	0.97	0.97	0
$\Delta T_{air,hx}$ (K)	0	0	—	3.87	3.88	−0.26
$T_{fuel,re}$ (K)	342.45	344.40	−0.57	357.25	351.89	1.52
$T_{fuel,engine}$ (K)	325.92	325.18	0.23	384.27	382.54	0.45
$T_{fuel,LP}$ (K)	328.60	327.77	0.25	391.90	389.69	0.57
$T_{fuel,HP}$ (K)	332.86	333.39	−0.16	393.94	392.88	0.27
$T_{fuel,SV}$ (K)	339.13	337.26	0.55	401.15	397.65	0.88

4 Results

To quantify the operational advantages of utilizing ram and secondary bypass air in an integrated thermal management system, four schemes with varying energy interaction frameworks are constructed in this study.

(1) **Scheme 1:** Serves as the baseline, exclusively using ram air to dissipate thermal loads from hot-return fuel.

(2) **Scheme 2:** Only secondary bypass air is employed as a heat sink to cool the hot-return fuel, and the area of the $HEX_{fuel-bypass\ air}$ is equal to that of the $HEX_{fuel-ram\ air}$.

(3) **Scheme 3:** Ram and secondary bypass air are used as heat sinks while maintaining the total area of heat exchangers.

(4) **Scheme 4:** Based on Scheme 1, the $HEX_{fuel-ram\ air}$ is preserved, secondary bypass air is introduced into the FTMS, and the heat transfer area of the $HEX_{fuel-bypass\ air}$ is equal to that of the $HEX_{fuel-ram\ air}$.

The design parameters of different schemes are listed in Table 9. The design point of the $HEX_{fuel-ram\ air}$ and $HEX_{fuel-bypass\ air}$ is the subsonic cruise condition, whose parameters are listed in Table 10. The design reference value K_{ram} and resistance coefficient of secondary bypass air ε_{air} are set to 200 $W \cdot m^{-2} \cdot K^{-1}$ and 1.5%, respectively.

Table 9
Design parameters of different schemes. The employed abbreviations are defined in the main text.

Scheme	A_{ram} (m^2)	A_{byp} (m^2)	A_{HEXs} (m^2)
1	0.50	0	0.5
2	0	0.50	0.5
3	0.25	0.25	0.5
4	0.50	0.50	1.0

Table 10
Design parameters of HEXs. The employed abbreviations are defined in the main text.

Type of HEXs	m_{fuel} ($kg \cdot s^{-1}$)	T_{fuel} (K)	p_{fuel} (MPa)	m_{air} ($kg \cdot s^{-1}$)	T_{air} (K)	p_{air} (kPa)
$HEX_{fuel-ram\ air}$	0.29	420	15	0.77	244.21	34.49
$HEX_{fuel-bypass\ air}$	0.29	420	15	11.70	303.08	59.71

The influence of the HEX flow arrangements on the FTMS performance is summarized in Table 11 for the subsonic cruise condition as an example. The results indicate that the heat transfer effectiveness of the parallel-flow type is 0.49% lower than that of cross-flow and counter-flow types. Additionally, the differences in the heat accumulation and return fuel temperature among the various flow arrangements are 0.7% and 0.1%, respectively. Based on these findings, the impacts of flow arrangements on overall FTMS performance could be considered negligible.

Table 11
Impacts of different flow arrangements on VCE and FTMS. The employed abbreviations are defined in the main text.

Flow arrangement	η_{ram} (%)	η_{byp} (%)	Q_{ram} (kW)	Q_{byp} (kW)	Q_{acc} (kW)	$T_{fuel,re}$ (K)
Parallel-flow	12.24	43.96	10.90	44.61	37.23	358.00
Cross-flow (n = 2)	12.29	44.20	10.92	44.84	36.98	357.70
Cross-flow (n = 4)	12.30	44.22	10.92	44.87	36.96	357.67
Cross-flow (n = 6)	12.30	44.23	10.92	44.87	36.95	357.66
Counter-flow	12.30	44.23	10.92	44.87	36.95	357.66

4.1 Comparison of different schemes during a typical flight mission

In this section, the variations in the heat dissipation and accumulation performance of the four schemes are examined during a ty[illegible]tion characteristics of each scheme and provides a quantitative characterization of their integrated performance throughout the flight mission. The VCE cycle parameters refer to the literature [40], and the flight mission to be analyzed is detailed in Table 12.

Table 12
Details of typical flight missions. The employed abbreviations are defined in the main text.

Mission number	Description	Duration (s)
1	Takeoff: H = 0 km, Ma_{to} = 0.2	10
2	Climbing and acceleration 1: H from 0 km to 5 km, Ma from 0.2 to 0.6	190
3	Climbing and acceleration 2: H from 5 km to 11 km, Ma from 0.6 to 0.8	200
4	Subsonic cruise: H = 11 km, Ma = 0.8	800
5	Horizontal acceleration: H = 11 km, Ma from 0.8 to 1.5	600
6	Supersonic cruise: H = 11 km, Ma = 1.5	200
7	Horizontal deceleration: H = 11 km, Ma from 1.5 to 0.8	200
8	Return to base: H from 11 km to 0 km, Ma from 0.8 to 0	1400

For the takeoff flight phase, Fig. 9(a) indicates that the heat dissipation of burning can reach approximately 200 kW, which is equal to the total heat load. The same results could be observed during flight phases such as climbing and acceleration, horizontal acceleration, and supersonic cruise. This result indicates that the cooling capability of the burning fuel is sufficient to address the heat loads, suggesting that none of these heat loads must be accumulated by the system. However, during the subsonic cruise and most of the return-to-base phases, heat dissipation of burning is notably weakened, with its value falling below 100 kW. Consequently, an extra heat sink should be introduced to enhance the system's cooling capability. If this is not implemented, some heat loads cannot be dissipated and will have to be accumulated in the system, leading to an increase in the temperature of the in-tank fuel.

The ram and secondary bypass air can serve as additional heat sinks when the cooling capability of the burning fuel is inadequate, with the latter option preferred. By comparing Figs. 9(b) and (c), it can be found that the secondary bypass air could address heat loads of 40 kW under the same heat transfer area, which is around 2.7 times higher than that of ram air. Therefore, heat accumulation can be reduced when the secondary bypass air acts as a cooling fluid. As indicated in Fig. 9(d), compared with the basic scheme, Schemes 2–4 could decrease the heat accumulation by approximately 50%, 32%, and 70%, respectively, during the subsonic cruise. In addition, the temperature of the secondary bypass air exceeds that of the fuel under the supersonic cruise, but its heat load could not be transferred into the FTMS, as none of the hot-return fuel flows into the $HEX_{fuel–bypass\ air}$. Therefore, the overall heat dissipation and accumulation characteristics of the FTMS could not be affected by the overtemperature of the secondary bypass air.

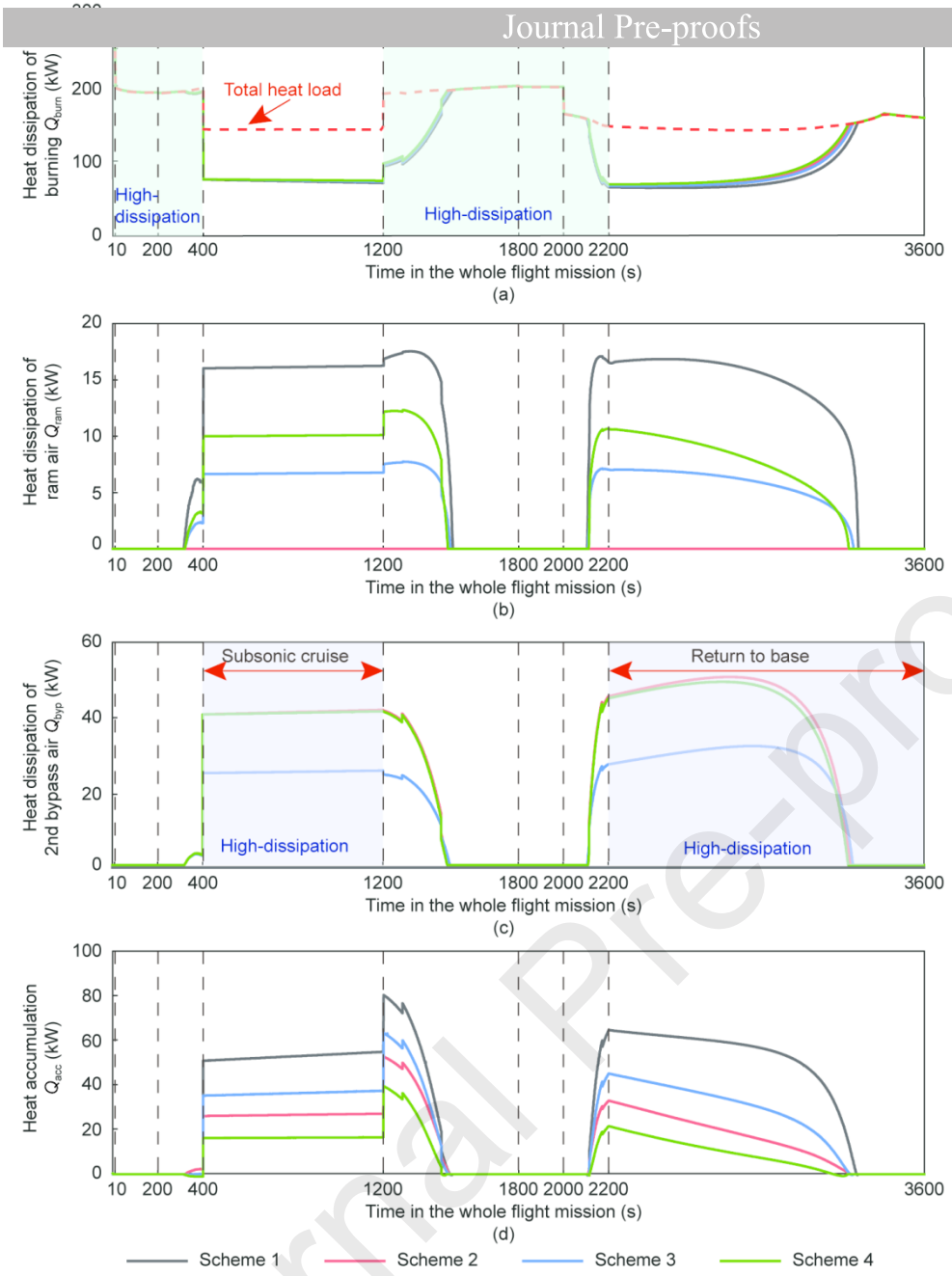

Fig. 9. Real-time variation of heat dissipation and accumulation. (a) Heat dissipation of burning; (b) heat dissipation of ram air; (c) heat dissipation of secondary bypass air; (d) heat accumulation.

The superiority of using secondary bypass air for heat dissipation can be further illustrated by assessing the heat accumulation throughout the entire flight mission by factoring in the flight time for each segment. As given in Figs. 10(a) and (b), the total heat dissipation of Scheme 1 exceeds 461.90 MJ, and its heat accumulation is 120.15 MJ. With the use of the $HEX_{fuel–bypass\ air}$, the improvement scheme notably increases heat dissipation and decreases heat accumulation. The heat accumulation of the advanced scheme is 31.17–76.21 MJ, reduced by 36.57%–74.06%. Generally, during the entire flight mission, the high heat-dissipation capability of burning fuel and secondary bypass air can complement each other, thereby enabling the system to utilize secondary bypass air to achieve excellent heat-dissipation performance.

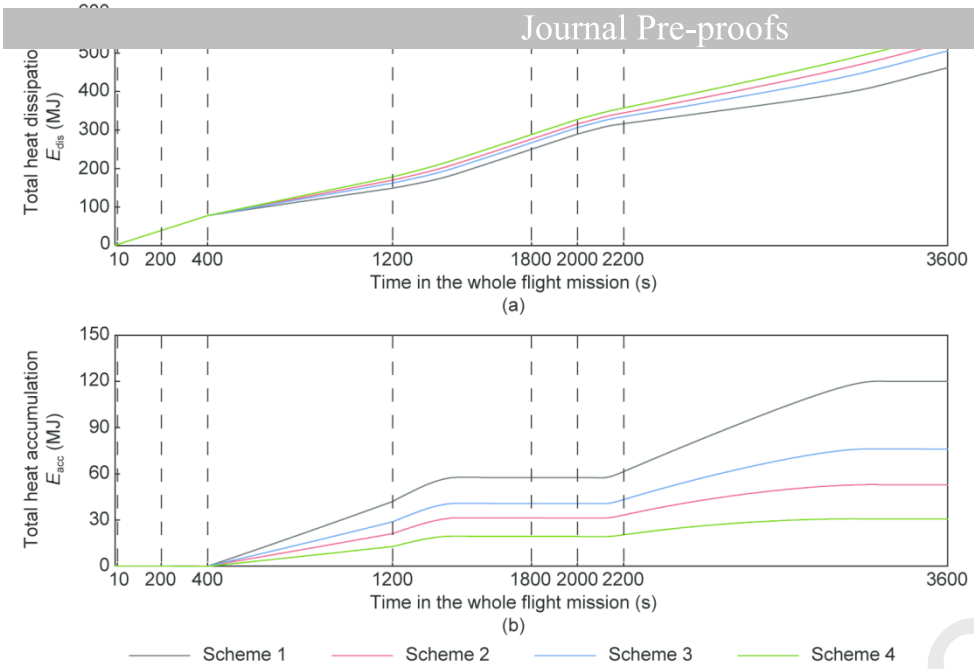

Fig. 10. Total heat dissipation and accumulation. (a) Total heat dissipation; (b) total heat accumulation.

Fig. 11 depicts the parameters of the return fuel and in-tank fuel during the flight mission, revealing the mechanism of reducing the heat accumulation of the VCE and FTMS by the secondary bypass air. As revealed in Figs. 11(a) and (b), owing to the increased heat transfer rate of the HEXs, the return fuel temperature can be reduced during the entire flight mission. Taking the subsonic cruise state as an example, the application of $HEX_{fuel–bypass\ air}$ reduces the return fuel temperature from 397.69 K to a range of 340.58–373.38 K. As the temperature of the return fuel decreases, the temperature rise of in-tank fuel notably decelerates. At the end of the flight mission, the in-tank fuel temperature of the advanced Schemes 2–4 reaches 314.42–322.84 K, which is significantly lower than that of the benchmark Scheme 1. This behavior signifies that a lower-temperature heat sink is available for the onboard equipment, which is conducive to extending its operational lifespan.

As given in Figs. 11 (c) and (d), under the same burning demand of the engine, the mass flow rate of the in-tank fuel remains nearly constant across the different schemes. This consistency is attributed to the fact that the thrust requirements and total heat load to be absorbed are identical for all schemes, resulting in a nearly constant demand for the total fuel supply. However, the mass flow rate of the return fuel decreases by 2.17%–4.10%, which is attributed to the reduced return fuel temperature. In general, the secondary bypass air effectively leverages the high mass flow rate and heat transfer coefficient of the $HEX_{fuel–bypass\ air}$ to affect the in-tank fuel temperature by reducing the mass flow and temperature of the return fuel, thereby decreasing the heat accumulation of the FTMS.

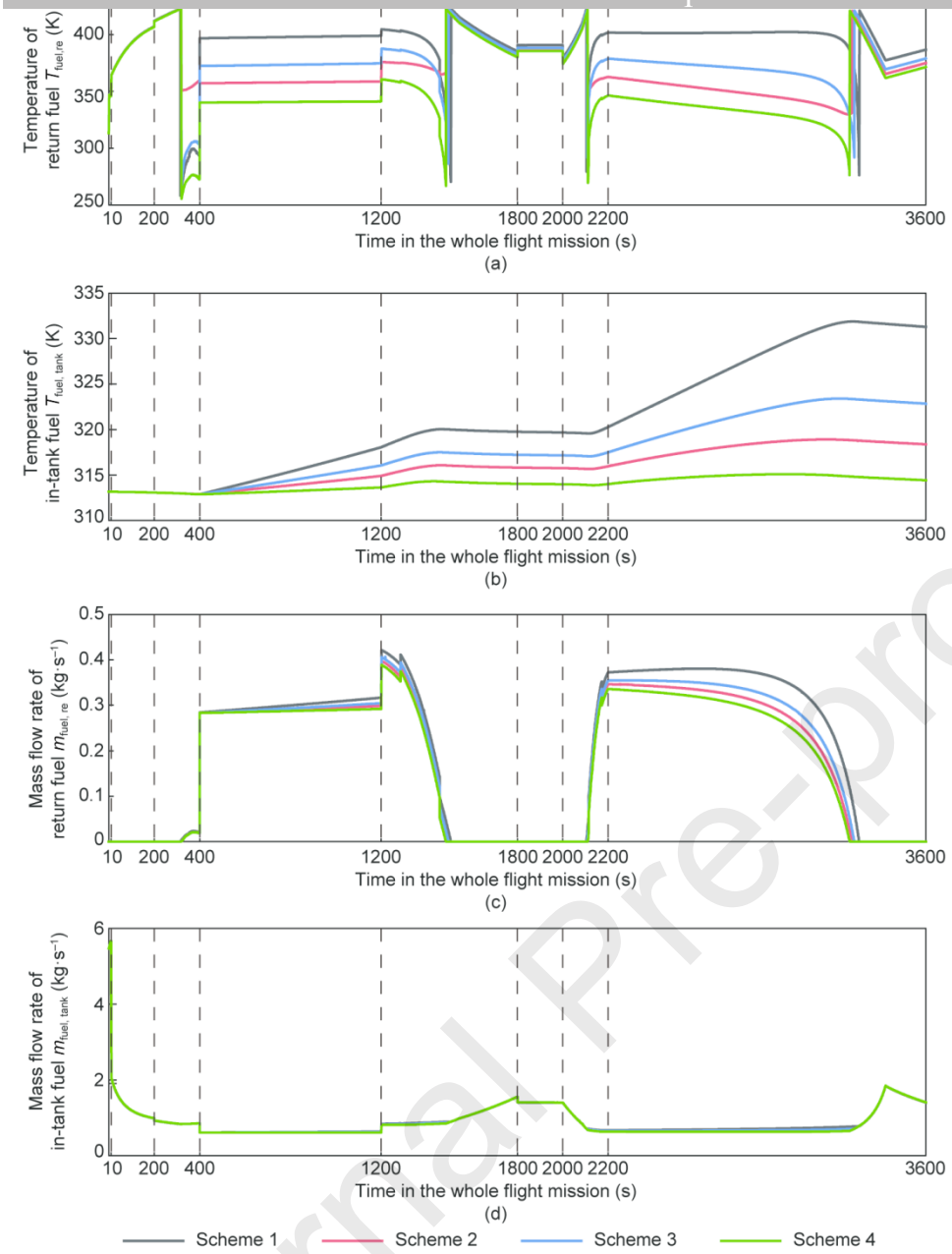

Fig. 11. Parameters of return fuel and in-tank fuel of the coupled system in the flight mission. (a) Temperature of return fuel; (b) temperature of in-tank fuel; (c) mass flow rate of return fuel; (d) mass flow rate of in-tank fuel.

Considering the evaluation indices of the FTMS, Fig. 12 presents the results of the performance evaluation of the coupled system. As the mission requirements of the VCE remain identical across all four schemes, so does the thrust, as illustrated in Fig. 12(a). Fig. 12(b) shows that the addition of $HEX_{fuel–bypass\ air}$ leads to a marginal increase of no more than 0.8% in SFC compared with benchmark Scheme 1. This slight increase in SFC is attributed to the pressure loss of the secondary bypass air flowing through the heat exchanger, which reduces the nozzle outlet pressure p_{out}. Consequently, additional fuel must be burned to maintain the required thrust based on Eq. (6).

The evaluation of the heat sink-cooling capability of the FTMS in Fig. 12(c) indicates that R_{EFF} trajectories are largely similar for all schemes, except for the divergence in the timing of the R_{EFF} peak during the return-to-base phase. This discrepancy is attributed to the use of secondary bypass air in Schemes 2–4, which effectively mitigates the heat accumulation compared with the baseline. A lower accumulation results in a reduced fuel inlet temperature (Fig. 11(b)), consequently enhancing the specific heat absorption capacity of the fuel and advancing the cessation of the return fuel flow, as illustrated in Fig. 11(c). Specifically, Scheme 4, with the largest A_{HEXs} and therefore providing the most effective return fuel cooling, reaches a peak value earliest at t = 3264 s. This value is lower than those obtained for Schemes 2 and 3 and the baseline value of t = 3306 s for Scheme 1. Furthermore, these differences in heat sink utilization directly translate to marked variations in the residual fuel-cooling capacity R_{RES}, with Scheme 4 performing the best, followed by Schemes 2 and 3; Scheme 1 is the worst, which is presented in Fig. 12(d). This variation aligns with the trend of the in-tank fuel temperature. In summary, under the condition of satisfying the thrust requirements for the flight mission, replacing ram air with secondary bypass air as the heat sink maintains the efficiency of fuel cooling and improves the cooling capacity of the remaining fuel during the flight mission at the cost of a small increase in SFC.

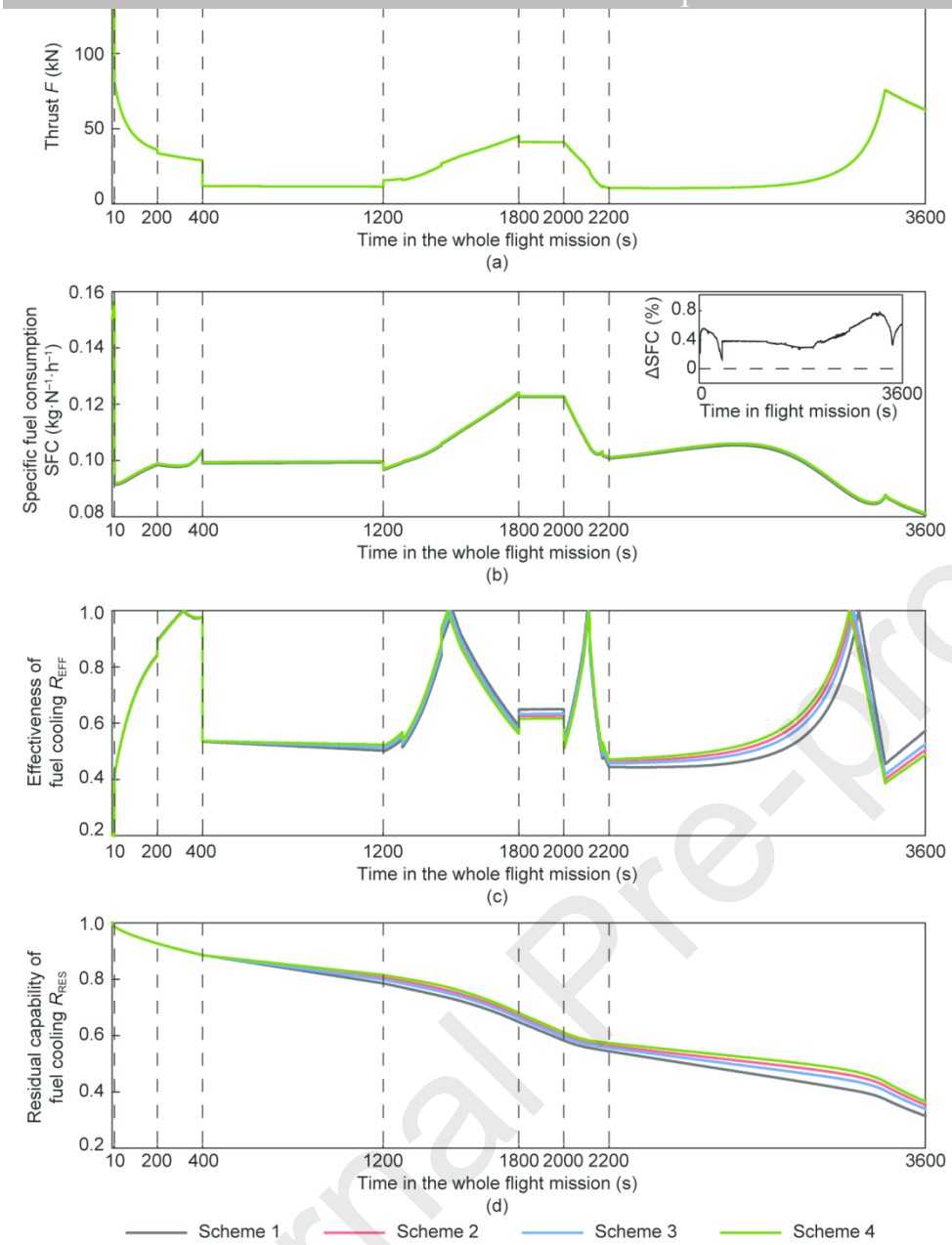

Fig. 12. Performance of the coupled system in the flight mission. (a) Thrust; (b) specific fuel consumption; (c) effectiveness of fuel cooling; (d) residual capability of fuel cooling.

Table 13 presents a comparison of the performance indices of the four schemes. The values of F, SFC, and R_{EFF} refer to the subsonic cruise state (t = 800 s), whereas R_{RES} and $T_{fuel,tank}$ are evaluated at the end-of-mission phase. As demonstrated in Table 13, for identical thrust requirements, the secondary bypass air enhances the utilization efficiency of the fuel heat sink by lowering the in-tank fuel temperature, thereby increasing the heat absorption potential of the FTMS and bolstering its robustness against off-design scenarios, such as unexpected transient thermal loads. This enhancement promotes the longevity of onboard equipment and extends the thermal endurance and mission capability of the aircraft. At the same heat transfer area, by replacing ram air with secondary bypass air, R_{EFF} and R_{RES} of the FTMS can be increased by 0.87% and 3.89%, respectively, while incurring only a marginal 0.4% increase in SFC. In summary, the secondary bypass air presents a practical auxiliary heat dissipation solution in the FTMS, avoiding high structural complexity and poor stealth performance of the aircraft.

Table 13
Comparative performance analysis of different schemes. The employed abbreviations are defined in the main text.

Scheme	Subsonic cruise F (kN)	Subsonic cruise SFC (kg·N^{-1}·h^{-1})	End of mission $T_{fuel,tank}$ (K)	Subsonic cruise R_{EFF} (%)	End of mission R_{RES} (%)
1	11.72	0.0991	331.28	51.84	31.43
2	11.72	0.0995	318.37	52.71	35.32
3	11.72	0.0995	322.84	52.49	33.91
4	11.72	0.0995	314.42	52.98	36.54

4.2 Characteristics of different schemes within the whole flight envelope

This section sheds light on how ram and secondary bypass air influence performance throughout the flight envelope and how [redacted] mes with different heat sinks are presented in Fig. 13.

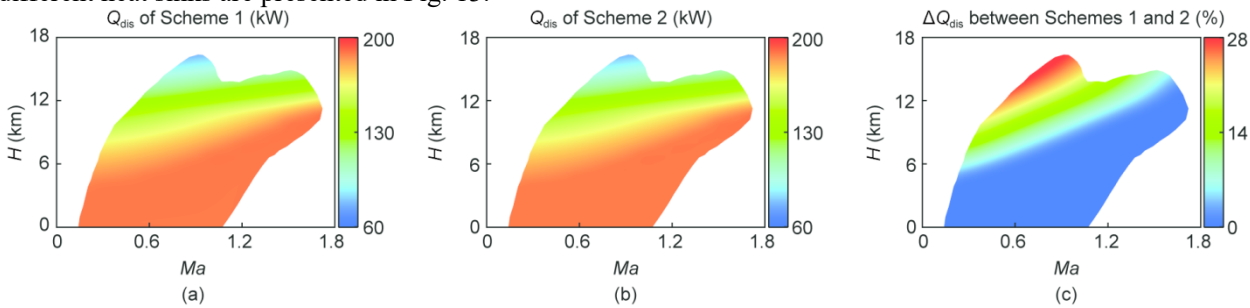

Fig. 13. Heat dissipation throughout the flight envelope. The employed abbreviations are defined in the main text. (a) Heat dissipation of Scheme 1; (b) heat dissipation of Scheme 2; (c) relative difference of heat dissipation between Schemes 1 and 2.

Within the low-altitude flight region, Schemes 1 and 2 exhibit similar heat-dissipation characteristics because all heat loads are discharged by fuel burning, eliminating the need for other heat sinks to provide cooling for the FTMS. By contrast, in high-altitude and low-speed flight region, the cooling capability of the burning fuel weakens, which increases the impact of the secondary bypass or ram air. The mass flow rate of the secondary bypass air exceeds that of the ram air, which leads to a higher heat transfer coefficient of the $HEX_{fuel–bypass\ air}$. Therefore, the cooling performance of Scheme 2 with secondary bypass air is 7%–28% higher than that of ram air, and this advantage is most pronounced at the top-left corner of the flight envelope.

As mentioned above, heat accumulation is only concomitant with hot-return fuel; therefore, the low-altitude flight region can be neglected, as it does not feature hot-return fuel (Figs. 14(a) and (b)). For the flight region characterized by the existence of hot-return fuel, two heat accumulation scenarios can be envisaged. When the temperature of the air exceeds that of the hot-return fuel, the heat loads are transferred from the former to the latter, but the increment of the heat accumulation is merely about 1 kW, occurring within the flight region defined between the orange dotted boundaries in Figs. 14(b) and (c). If the opposite circumstance occurs, the sufficient cooling capability of the secondary bypass air significantly reduces the heat accumulation, and its maximum value can reach approximately 50% across the entire flight envelope. Overall, the secondary bypass air is more advantageous than ram air for mitigating heat loads in high-altitude flight region.

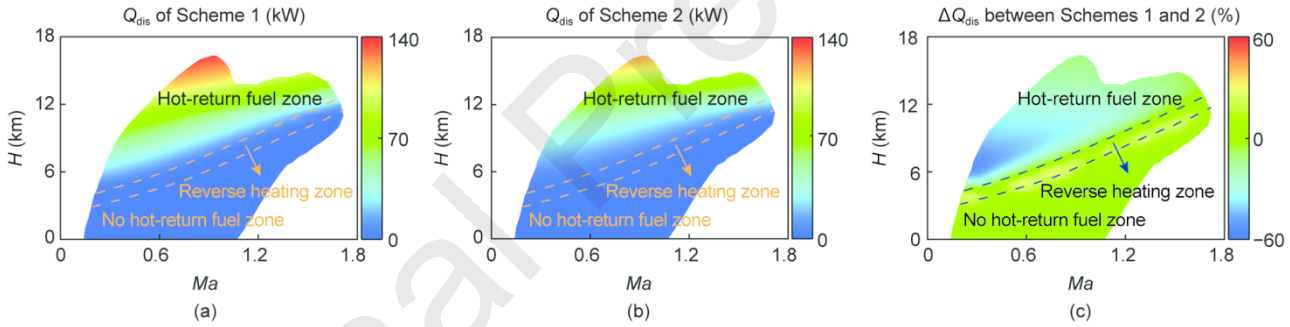

Fig. 14. Heat accumulation throughout the flight envelope. The employed abbreviations are defined in the main text. (a) Heat accumulation of Scheme 1; (b) heat accumulation of Scheme 2; (c) relative difference of heat accumulation between Schemes 1 and 2.

Fig. 15 and Fig. 16 describe the variations of the specific fuel consumption and effectiveness of fuel cooling throughout the flight envelope, respectively. Compared with Scheme 1, the SFC in Scheme 2 increases slightly by 0.26%–0.74%, as more fuel must be combusted to mitigate the thrust loss caused by the pressure loss of the $HEX_{fuel–bypass\ air}$. In the entire flight envelope, two zones can be identified based on the change in R_{EFF} (Fig. 16). In low-altitude area, hot-return fuel is not required. As the total fuel flow demanded of the FTMS increases, the fuel combustion temperature $T_{fuel,b}$ decreases for a given heat load, leading to a decline in R_{EFF}. Above the reverse heating zone, the slight increase in R_{EFF} is due to an increase in the proportion of fuel for combustion relative to the total supplied flow. This reduces the reliance on return fuel for cooling, allowing a larger fraction of the heat load to be dissipated through burning. This effect becomes more pronounced in high-altitude and low-speed region. In general, the FTMS incorporating secondary bypass air achieves a higher R_{EFF} with a lower fuel consumption cost in high-altitude and low-speed region.

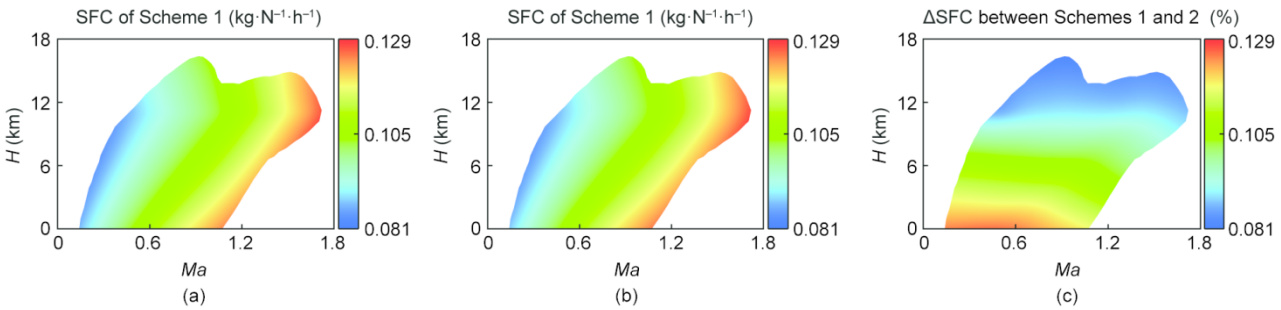

Fig. 15. Specific fuel consumption throughout the flight envelope. The employed abbreviations are defined in the main text. (a) Specific fuel cons[Journal Pre-proofs]1 and 2.

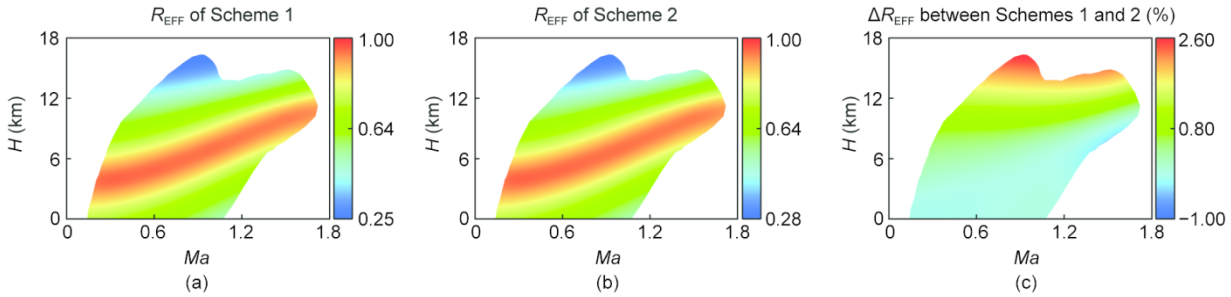

Fig. 16. Effectiveness of fuel cooling throughout the flight envelope. The employed abbreviations are defined in the main text. (a) Fuel cooling effectiveness of Scheme 1; (b) fuel cooling effectiveness of Scheme 2; (c) relative difference of fuel cooling effectiveness between Schemes 1 and 2.

4.3 Optimization of total heat transfer area allocation

This section aims to optimize the utilization of the secondary bypass and ram air to enhance the heat-dissipation capability of the FTMS. A parametric analysis is first conducted to identify the most influential design variables, followed by an optimization study to derive the best solution. Boundary conditions such as the thermodynamic parameters of the secondary bypass and ram air, can be determined by the flight mission. The subsonic cruise and return-to-base segments have been selected, considering that the heat-dissipation capability of the FTMS is especially important for low-fuel-consumption flight mission segments. The variables involved in the parameter sensitivity analysis are listed in Table 14, including the total heat transfer area A, heat transfer coefficient K_{ram}, allocation ratio of the heat transfer area R_A, and resistance coefficient ε_{air}. R_A represents the area ratio of the $\text{HEX}_{\text{fuel–bypass air}}$ and $\text{HEX}_{\text{fuel–ram air}}$, which can be obtained as follows:

$$R_A = \frac{A_{\text{byp}}}{A_{\text{ram}}} \quad (56)$$

Table 14
Reference values and variation ranges of independent variables.

Independent variable	Reference	Variable range
Total heat transfer area A (m^2)	0.5	[0, 1]
Heat transfer coefficient K_{ram} ($\text{W}\cdot\text{m}^{-2}\cdot\text{K}^{-1}$)	200	[0, 400]
Allocation ratio of heat transfer area R_A	0.5	[0, 1]
Resistance coefficient ε_{air}	1.5%	[0, 3%]

Fig. 17 presents the sensitivity of the coupled system performance to several key design variables under subsonic cruise and return-to-base conditions. As depicted in Fig. 17(a), both the total heat transfer area A and the heat transfer coefficient K_{ram} exhibit comparable and significant impacts on heat accumulation. Specifically, a 100% increase in either A or K_{ram} leads to a 58% reduction in heat accumulation. Conversely, a substantial reduction in these parameters significantly increases the heat accumulation, which is proportional to the reduction in the heat-dissipation capability. This behavior is attributed to the direct proportionality of both parameters to the number of transfer units NTU. As NTU is the sole determinant of heat exchanger effectiveness η when other factors are held constant, any change in A or K_{ram} exerts a commensurate influence on heat dissipation. Furthermore, the allocation ratio of the heat transfer area R_A also plays a crucial role. As R_A varies from minimum to maximum, the heat accumulation decreases from 48% to 28%. This indicates that a higher R_A directs a larger portion of the available heat transfer area to the secondary bypass air, which serves as a more effective heat sink, thereby enhancing heat dissipation. Among the investigated parameters, the resistance coefficient demonstrates a negligible impact on heat accumulation (< 1%). In summary, augmenting the heat transfer coefficient and area of heat exchangers is the most direct strategy for improving the heat dissipation of the return fuel.

Fig. 17(b) illustrates the sensitivity of the specific fuel consumption to the same set of variables. The influences of A, K_{ram}, and R_A on SFC are modest and virtually identical, resulting in a decrease of SFC by 0.1% as these parameters are varied across their full ranges. This marginal improvement is attributed to the energy recovered into the secondary bypass air, which slightly lessens the fuel burn required for a given thrust. By contrast, the resistance coefficient displays a stronger correlation to the specific fuel consumption, with the SFC increasing by 0.95% when the resistance coefficient rises from 1.5% to 3%. These results indicate that the flow resistance of the heat exchangers in the secondary bypass must be considered to achieve performance synergy between the VCE and FTMS. The results presented in Figs. 17(c) and (d) further reveal that the influence of all independent variables on the VCE–FTMS performance follows a consistent pattern despite the variations in the mass flow rate of the secondary bypass air across different flight conditions. Specifically, varying A or K_{ram} significantly influences the heat accumulation of the FTMS, resulting in fluctuations ranging from −38% to 55%. This fluctuation range is narrower than that observed for subsonic cruise, which is attributed to a higher baseline of heat accumulation under this condition. Furthermore, as illustrated in Fig. 17(d), similar to the subsonic cruise condition, SFC is mainly affected by the resistance coefficient but with a more pronounced variation. This pronounced variation is attributed to the higher proportion of secondary bypass air relative to the total inlet airflow at this state. This increased bypass ratio makes the thrust more sensitive to pressure losses in the bypass duct. Consequently, more fuel is required to maintain the target thrust.

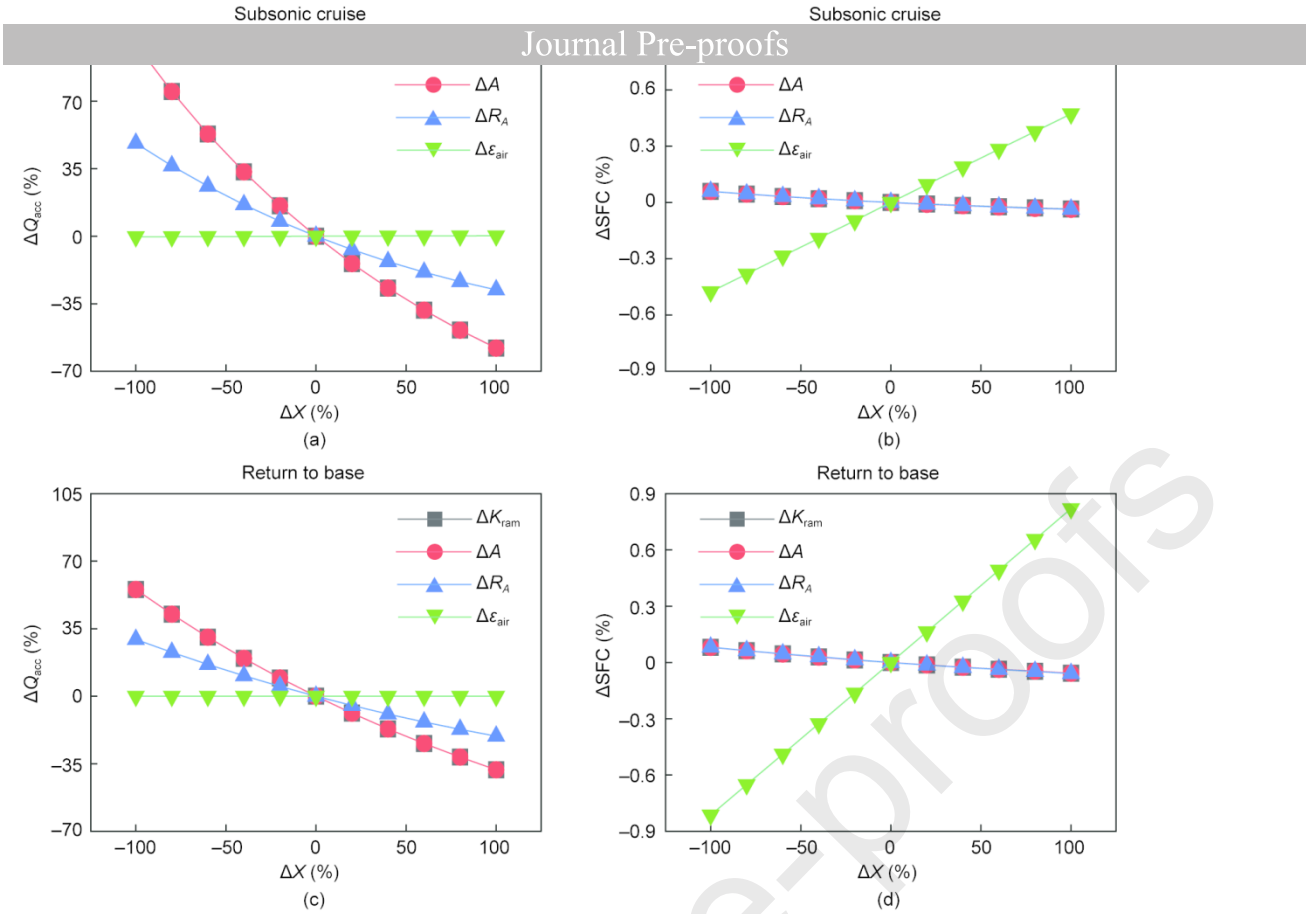

Fig. 17. Effects of independent variables on the performance of the coupled system. The employed abbreviations are defined in the main text. Relative rate of change of (a) heat accumulation under subsonic cruise, (b) specific fuel consumption under subsonic cruise, (c) heat accumulation under return to base, and (d) specific fuel consumption under return to base.

The influence patterns of each parameter on the system performance are consistent across different airflow rates, and the preceding sensitivity analysis reveals that SFC is predominantly influenced by the resistance coefficient. Therefore, in the subsequent analysis, the resistance coefficient is held constant at its baseline value, and the focus is shifted to investigating the mechanisms through which the remaining independent variables affect the heat accumulation of the FTMS under a subsonic cruise state. As illustrated in Fig. 18, the heat accumulation trend closely mirrors the temperature of the hot-return fuel, and the capacity of heat accumulation could be reduced effectively by increasing the total heat transfer area or heat transfer coefficient. This finding is consistent with the results of the parameter sensitivity analysis, indicating that within a constrained design space for HEXs, enhancing the heat transfer area and heat transfer coefficient is crucial for performance improvement.

To further investigate the underlying mechanism through which the heat transfer area ratio influences thermal accumulation, the heat transfer coefficient is set to a representative value of 400 $W \cdot m^{-2} \cdot K^{-1}$. When the total heat transfer area is set to 0.25 m^2 or 0.50 m^2, the heat accumulation and the hot-return fuel temperature decrease with the increasing heat transfer area ratio (Fig. 19), which indicates that fully using secondary bypass air is the best way of dissipating heat loads. The reason is that the heat transfer coefficient of the $HEX_{fuel–bypass\ air}$ exceeds that of the $HEX_{fuel–ram\ air}$, and a greater heat load can be dissipated when the heat transfer area is allocated to the $HEX_{fuel–bypass\ air}$.

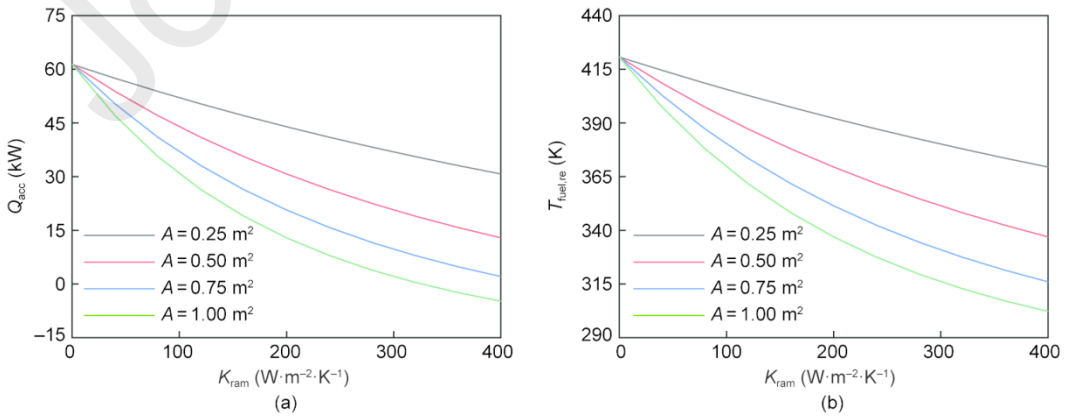

Fig. 18. Effects of the heat transfer coefficient on heat-accumulation performance. The employed abbreviations are defined in the main text. (a) Heat accumulation; (b) temperature of return fuel.

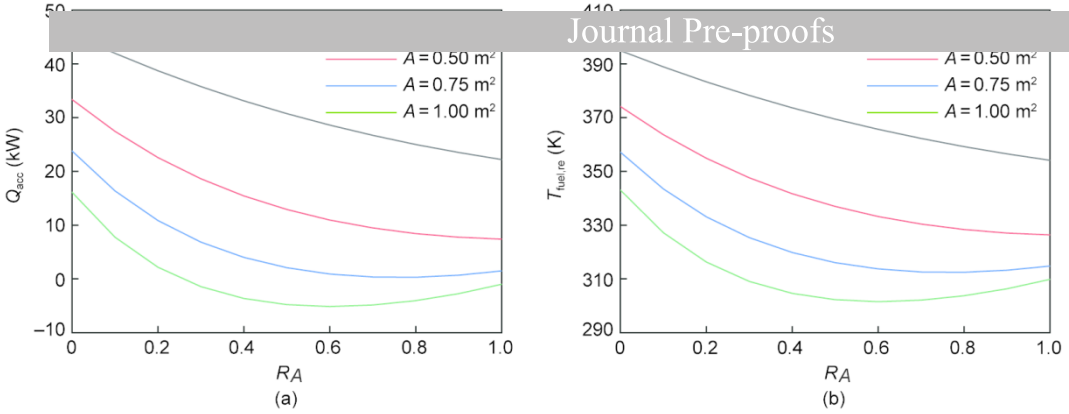

Fig. 19. Effects of the heat transfer area ratio on heat-accumulation performance. The employed abbreviations are defined in the main text. (a) Heat accumulation; (b) temperature of return fuel.

Although $HEX_{fuel–bypass\ air}$ exhibits a higher heat transfer coefficient, indiscriminately maximizing R_A may compromise the overall heat-dissipation performance of the FTMS, particularly when the total heat transfer area is large, as demonstrated in Fig. 19 for A = 0.75 m^2 or 1.00 m^2. This phenomenon occurs because with a sufficiently large heat transfer area A_{byp}, the temperature of the hot fuel after cooling progressively approaches the inlet temperature of the bypass air. This reduces the heat transfer temperature difference, notably decelerating the increase in the heat transfer rate with respect to A_{byp}. In this situation, a certain heat transfer area should be applied to the $HEX_{fuel–ram\ air}$. For A = 1.00 m^2, the optimal R_A is 0.6, and $T_{fuel,re}$ at R_A = 0.6 (301.51 K) is 2.68% lower than that at R_A = 1 (309.82 K). Therefore, when the total heat transfer area is sufficiently large, ram air should be utilized as an additional heat sink for fuel cooling, whereas ram air is not required if the heat transfer area is limited.

5 Conclusions

In this work, an integrated multi-level analysis model is proposed to simultaneously consider the mass/energy interactions between the VCE and FTMS. Based on an integrated simulation of a typical flight mission and envelope, a systematic investigation has been conducted between a traditional FTMS scheme utilizing ram air and a novel approach using secondary bypass air. The primary conclusions are listed as follows:

(1) Within a typical flight mission, secondary bypass air demonstrates a cooling capability superior to that of ram air and can seamlessly complement burning fuel, thereby addressing the problem of insufficient heat dissipation in the FTMS under subsonic cruise and other low-fuel-consumption flight phases. The thermal accumulation can be reduced by 36.57%–74.06%, which coincides with a decrease in the hot-return fuel flow of 2.17%–4.10% in the subsonic cruise state.

(2) Throughout the flight envelope, the secondary bypass air exhibits superior heat-dissipation performance in high-altitude and low-speed flight region, and the capacity of thermal dissipation exceeds that of ram air by 7%–28%. Besides, the rise in specific fuel consumption induced by $HEX_{fuel–ram\ air}$ and $HEX_{fuel–bypass\ air}$ is at the same level, with a relative difference ranging from 0.26% to 0.74%.

(3) The total heat transfer area, heat transfer coefficient, and allocation ratio of the heat transfer area strongly impact the heat dissipation and accumulation performance of the FTMS. Under a restricted total heat transfer area, our findings suggest that the area should be allocated to the secondary bypass air, hence the optimal ratio of the heat transfer area is equal to one. If the total heat transfer area is large, parts of the area should be distributed to the secondary bypass air for fully utilizing its cooling capability, and the remaining parts need to be employed by ram air for further improving heat dissipation.

In summary, by quantitatively validating the coupling between the secondary bypass air in the VCE and the FTMS, this work establishes a foundation for the development of an integrated thermal management scheme for advanced fighter aircraft and engine design. Despite the promising advancements presented, the current model exhibits several limitations that necessitate further investigation. The model's current emphasis on mass and energy interactions, coupled with simplified flow resistance models and a preset control strategy dictated by the maximum fuel temperature, restricts its predictive power and adaptability. Our research will focus on developing and evaluating a model predictive control (MPC) strategy to dynamically optimize the variable area bypass injector of the VCE and the return fuel flow of the FTMS across the full flight envelope. Such an approach aims to overcome the limitations of static control and achieve an optimal tradeoff between the fuel consumption of the VCE and the heat-dissipation performance of the FTMS. Additionally, Hardware-in-the-loop experiments will be conducted to rigorously validate the effectiveness of the proposed MPC method, thereby establishing a foundation for next-generation thermal management systems.

Acknowledgements

The authors appreciate the supports from the China Postdoctoral Fellowship Program of CPSF (CZC20233372) and the Fundamental Research Funds for the Central Universities (501QYZX2023146001).

Nomenclature

A	Area, m^2
C	Empirical constant
CDFS	Core-driven fan stage
D	Drag, kN
DI	External store drag coefficient
E	Energy, MJ
F	Thrust, kN
Gr	Grashof number
H	Height, km
HEX	Heat exchanger
HL	Heat load
HP	High-pressure pump
HPC	High-pressure compressor
HPT	High-pressure turbine
K	Heat transfer coefficient, $W \cdot m^{-2} \cdot K^{-1}$
L	Lift, kN
LHV	Lower heating value, $J \cdot kg^{-1}$
LP	Low-pressure pump
LPT	Low-pressure turbine
M	Mass, kg
Ma	Mach number
N	Relative rotation speed
NTU	Number of transfer units
Nu	Nusselt number
Pr	Prandtl number
Q	Heat transfer rate, kW
R	Ratio
Re	Reynolds number
R_g	Gas constant, $J \cdot kg^{-1} \cdot K^{-1}$
SFC	Specific fuel consumption, $kg \cdot N^{-1} \cdot h^{-1}$
SV	Servo actuation
T	Temperature, K
V	Velocity, $m \cdot s^{-1}$
W	Power, kW
c_p	Specific heat capacity, $J \cdot kg^{-1} \cdot K^{-1}$
d	Diameter, m
e	Error value
f	Fuel-to-air ratio
g	Acceleration of gravity, $m \cdot s^{-2}$

h	Specific enthalpy, J·kg^{-1}
k	Specific heat ratio
m	Mass flow rate, kg·s^{-1}
n	Factor
p	Pressure, kPa
q	Dynamic pressure, kPa
r	Recovery factor
s	Specific entropy, J·kg^{-1}·K^{-1}
t	Time, s
x	Exponent of Re
y	Exponent of Pr

Greek symbols

α	Convective heat transfer coefficient, W·m^{-2}·K^{-1}
β	Auxiliary line index
ε	Resistance coefficient
φ	Correction of specific heat capacity
η	Efficiency
θ	Blade angle
λ	Conductivity, W·m^{-1}·K^{-1}
μ	Dynamic viscosity, kg·m^{-1}·s^{-1}
ξ	Proportion
π	The ratio of pressure
ρ	Density, kg·m^{-3}
σ	Pressure recovery coefficient

Subscripts

EFF	Efficiency
H	High
L	Low
RES	Residual capability
Ab	Afterburner
acc	Accumulation
avi	Avionics system
aw	Adiabatic wall
b	Burner
ble	Bleeding
c	Cold
co	Counter-flow
com	Component
cri	Critical
cro	Cross
des	Design

dis	Dissipation
E	Environment
ecs	Environmental control system
f	Flow
h	Hot
hx	Heat exchanger
hyd	Hydraulic system
i	Index
id	Ideal
in	Inlet
o	Overload
off	Off-design
out	Outlet
P	Pump
pa	Parallel-flow
pro	Propulsion
r	Request
re	Return
ref	Reference
s	Supply
stan	Standard
t	Total
to	Takeoff

References

[1] Wang B, Zhao H, Yu L, Ye Z. Study of temperature effect on servovalve-controlled fuel metering unit. J Eng Gas Turbine Power 2015;137(6):061503.
[2] Fan H, Piao Y. Cooling design of an aero-engine fuel centrifugal pump at shut-off. Adv Mech Eng 2017;9(6):1687814017709700.
[3] Ebrahimi A, Jafari S, Nikolaidis T. Heat load development and heat map sensitivity analysis for civil aero-engines. Int J Turbomach Propuls Power 2024;9(3):25.
[4] Aygun H, Cilgin ME, Ekmekci I, Turan O. Energy and performance optimization of an adaptive cycle engine for next generation combat aircraft. Energy 2020;209:118261.
[5] Chen H, Zheng Q, Gao Y, Zhang H. Performance seeking control of minimum infrared characteristic on double bypass variable cycle engine. Aerosp Sci Technol 2021;108:106359.
[6] Sprouse JG. F-22 environmental control/thermal management system design optimization for reliability and integrity-a case study. In: SAE technical paper 961339. Warrendale: SAE International; 1996.
[7] Tao Z, Fu Y, Xu G, Deng H, Jia Z. Experimental study on influences of physical factors to supercritical RP-3 surface and liquid-space thermal oxidation coking. Energy Fuels 2014;28(9):6098–106.
[8] Huang H, Spadaccini LJ, Sobel DR. Fuel-cooled thermal management for advanced aeroengines. J Eng Gas Turbine Power 2004;126(2):284–93.
[9] Lira A, Juarez R, Petersen EL, Loebick C. An experimental apparatus for controlled measurements to study fuel coking deposition at high temperatures. In: Proceedings of the AIAA SCITECH 2025 Forum; 2025 Jan 06–10; Orlando, FL, USA. Reston: American Institute of Aeronautics and Astronautics (AIAA); 2025. p. 0745.
[10] van Heerden AS, Judt DM, Jafari S, Lawson CP, Nikolaidis T, Bosak D. Aircraft thermal management: practices, technology, system architectures, future challenges, and opportunities. Prog Aerosp Sci 2022;128:100767.
[11] Jasa JP, Mader CA, Martins JR. Trajectory optimization of a supersonic aircraft with a thermal fuel management system. In: Proceedings of the 2018 Multidisciplinary Analysis and Optimization Conference; 2018 Jun 25–29; Atlanta, GA, USA. Reston: American Institute of Aeronautics and Astronautics Inc.; 2018. p. 3884.
[12] Coutinho M, Bento D, Souza A, Cruz R, Afonso F, Lau F, et al. A review on the recent developments in thermal management systems for hybrid-electric aircraft. Appl Therm Eng 2023;227:120427.
[13] Kellermann H, Habermann A, Vratny P, Hornung M. Assessment of fuel as alternative heat sink for future aircraft. Appl Therm Eng 2020;170:114985.
[14] German BJ. Tank heating model for aircraft fuel thermal systems with recirculation. J Propuls Power 2012;28(1):204–10.
[15] Shi M, Gladin J, Mavris DN. A systematic methodology for populating the aircraft thermal management system architecture space. In: Proceedings of the AIAA SCITECH 2021 Forum; 2021 Jan 11–15; virtual event. Reston: American Institute of Aeronautics and Astronautics (AIAA); 2021. p. 1295.
[16] Sigthorsson D, Oppenheimer MW, Doman DB. Aircraft thermal endurance enhancement using a dual tank configuration and temperature regulation. In: Proceedings of the 2018 AIAA Guidance, Navigation, and Control Conference; 2018 Jan 08–12; Kissimmee, FL, USA. Reston: American Institute of Aeronautics and Astronautics (AIAA); 2018. p. 0612.
[17] Sigthorsson D, Oppenheimer MW, Doman DB. Flex versus dual tank thermal management systems. In: Proceedings of the AIAA SCITECH 2023 Forum; 2023 Jan 23–27; National Harbor, MD, USA. Reston: American Institute of Aeronautics and Astronautics (AIAA); 2023. p. 1045.
[18] Sigthorsson D, Oppenheimer MW, Doman DB. N-tank thermal management system framework for thermal endurance enhancement. In: Proceedings of the AIAA SCITECH 2022 Forum; 2022 Jan 03–07; San Diego, CA, USA. Reston: American Institute of Aeronautics and Astronautics (AIAA); 2022. p. 0750.

[19] Sigthorsson D, Oppenheimer MW, Doman DB. N-tank continuous framework for thermal management to enhance thermal endurance. In: Proceedings of the AIAA
[20] Huang GF, Doman DB, Oppenheimer MW, Tipton A, Sigthorsson DO. Control of a switched mode fuel thermal management system. J Thermophys Heat Trans 2022;36(1):13–27.
[21] Xu J, Wang R, Zhang Q, Cui T, Li H, Pei L, et al. Design of engine cooling system using improved particle swarm optimization algorithm. IEEE Sens J 2023;23(17):19060–72.
[22] Sigthorsson D, Oppenheimer MW, Doman DB. Flight endurance enhancement via thermal management system control subject to multiple limitations. In: Proceedings of the AIAA SCITECH 2020 Forum; 2020 Jan 06–10; Orlando, FL, USA. Reston: American Institute of Aeronautics and Astronautics (AIAA); 2020. p. 1825.
[23] Doman DB. Rapid mission planning for aircraft thermal management. In: Proceedings of the AIAA Guidance, Navigation, and Control Conference; 2015 Aug 05–08; Boston, MA, USA. Reston: American Institute of Aeronautics and Astronautics (AIAA); 2015. p. 1076.
[24] Doman DB. Fuel flow topology and control for extending aircraft thermal endurance. J Thermophys Heat Trans 2018;32(1):35–50.
[25] Wang H, Li P, Xiao H, Zhou X, Lei R. Intelligent energy management for solar-powered unmanned aerial vehicle using multi-objective genetic algorithm. Energy Convers Manage 2023;280:116805.
[26] Yang S, Lin Y, Yu H, Xu X, Liang X. Thermal management of fuel heat sink in aircraft via flow path optimization. Appl Therm Eng 2024;246:122880.
[27] Xu Y, Yan Z, Xia W. A novel system for aircraft cabin heating based on a vapor compression system and heat recovery from engine lubricating oil. Appl Therm Eng 2022;212:118544.
[28] Chen W, Wang R, Li X, Lu S, Fang X. Study of the heat transfer design of an integrated thermal management system for hypersonic vehicles using supercritical nitrogen as expendable coolant. Aerosp Sci Technol 2022;123:107440.
[29] Johnson DJ, Niedbalski NP, Ervin JS, Patnaik SS. A thermal management system using ammonium carbamate as an endothermic heat sink. Appl Therm Eng 2017;121:897–907.
[30] Wang Y, Xu Z, Wang H, Qiu Y, Cheng X, Bai J. Enhancing aerodynamic performance by waste heat in a hydrogen fuel cell powered aircraft. Appl Therm Eng 2024;254:123873.
[31] Corbett M. Shaft power extraction and waste heat rejection using a three stream variable cycle engine. SAE Int J Aerosp 2012;5(2012-01-2167):371–85.
[32] Dooley M, Lui N, Newman R, Lui C. Aircraft thermal management-heat sink challenge. Warrendale: SAE International; 2014.
[33] Simmons RJ. Design and control of a variable geometry turbofan with an independently modulated third stream [dissertation]. Columbus: The Ohio State University; 2009.
[34] Clark RA, Shi M, Gladin J, Mavris D. Design and analysis of an aircraft thermal management system linked to a low bypass ratio turbofan engine. J Eng Gas Turbine Power 2022;144(1):011019.
[35] Walsh PP, Fletcher P. Gas turbine performance. Hoboken: John Wiley & Sons; 2004.
[36] Xu G, Jia Z, Wen J, Deng H, Fu Y. Thermal-conductivity measurements of aviation kerosene RP-3 from (285 to 513) K at sub- and supercritical pressures. Int J Thermophys 2015;36(4):620–32.
[37] Fu Y, Gang X, Zhi H, Liu Y, Xu G. Isobaric specific heat capacity measurement in the trans-critical temperature regions for kerosene RP-3 under pressures of 6–8 MPa. J Chem Eng Data 2024;69(11):3730–8.
[38] Fu Y, Liu W, Shi S, Wang R, Liu Y, Xu G. Density measurements of aviation kerosene RP-3 over temperature range from 323 K to 783 K under supercritical pressures from 6 MPa to 8 MPa. Chin J Aeronauti 2025;38(7):103474.
[39] Liu Y, Xu G, Shi S, Wang R, Fu Y. Viscosity measurements of endothermic propellant EHF-TU and aviation kerosene RP-3 under supercritical pressures. J Chem Eng Data 2025;70(2):827–34.
[40] Huang C, Xu G, Wen J, Li M, Zhuang L. Performance advantage evaluation of air–oil heat exchanger based on variable cycle engine in flight mission. In: Proceedings of the ASME International Mechanical Engineering Congress and Exposition; 2022 Oct 30–Nov 3; Columbus, OH, USA. New York City: American Society of Mechanical Engineers (ASME); 2022. V008T011A025.
[41] Cengel YA, Boles MA. Thermodynamics: an engineering approach. 7th ed. New York City: McGraw Hill; 2011.
[42] Yang S, Tao W. Heat transfer. Beijing: Higher Education Press; 2006. Chinese.
[43] Sojoudi A, Nourbakhsh A, Shokouhmand H. Experimental evaluation of temperature rise in centrifugal pumps at partial flow rates. J Braz Soc Mech Sci Eng 2018;40(4):183.
[44] Cengel YA, Boles MA. Engineering thermodynamics. 7nd ed. Shen W, Tong J, translators. Beijing: Higher Education Press; 2016.
[45] Zhuang L, Xu G, Dong B, Liu Q, Huang C, Wen J. Study on performance and mechanisms of a novel integrated model with power & thermal management system and turbofan engine. Appl Therm Eng 2023;219:119481.
[46] Sekulic DP, Sekulic DP. Fundamentals of heat exchanger design. Hoboken: John Wiley & Sons; 2003.
[47] Sha Z. Aircraft design manual. Beijing: Aerospace Industry Press; 2005. Chinese.
[48] Mattingly JD. Aircraft engine design. 2nd ed. Reston: American Institute of Aeronautics and Astronautics (AIAA); 2002.
[49] Shou R, He H. Aircraft environmental control. Beijing: Beihang University Press; 2004. Chinese.
[50] Tipton R, Figliola RS, Ochterbeck JM. Thermal optimization of the ECS on an advanced aircraft with an emphasis on system efficiency and design methodology. In: SAE technical paper 971241. Warrendale: SAE International; 1997.
[51] Tang M, Ji H, Hu Y. Optimal design of comprehensive thermal management system for supersonic vehicle. J Propuls Technol 2022;43(1):50–60. Chinese.

Declaration of Interest Statement

☼ The authors declare that they have no known competing financial interests or personal relationships that could have appeared to influence the work reported in this paper.

☐ The author is an Editorial Board Member/Editor-in-Chief/Associate Editor/Guest Editor for this journal and was not involved in the editorial review or the decision to publish this article.

☐ The authors declare the following financial interests/personal relationships which may be considered as potential competing interests: